JET IMPINGEMENT COOLING OF RECTIFIER DIODES FOR AEROSPACE GENERATORS

by

Sushant Poudel

Submitted in Partial Fulfillment of the Requirements
for the Degree of
Master of Science in Engineering
in the
Mechanical Engineering

Program

YOUNGSTOWN STATE UNIVERSITY

August 2023

JET IMPINGEMENT COOLING OF RECTIFIER DIODES FOR AEROSPACE GENERATORS

Sushant Poudel

I hereby release this thesis to the public. I understand that this thesis will be made available from the OhioLINK ETD Center and the Maag Library Circulation Desk for public access. I also authorize the University or other individuals to make copies of this thesis as needed for scholarly research.

Signature:

Sushant Poudel, Student Date

Approvals:

Stefan I. Moldovan, Thesis Advisor Date

Kyosung Choo, Committee Member Date

Virgil C. Solomon, Committee Member Date

Dr. Salvatore A. Sanders, Dean of Graduate Studies Date

Abstract

This thesis focuses on the thermal management using jet cooling for rectifier diodes used in the aerospace industry. Jet impingement cooling is an excellent method to dissipate heat from electronic components considering its high heat transfer efficiency. To investigate the feasibility and effectiveness of jet cooling in maintaining the temperature of rectifier diodes within acceptable limits under aerospace operating conditions, the study consisted of two phases: a preliminary examination using a simplified model to determine the suitable nozzle size, number of nozzles, and the nozzle configuration, followed by a compressive analysis on the real diodes to evaluate the cooling performance using the identified optimal parameters.

In the preliminary study, a simplified diode model and a proposed bus bar were utilized to understand the impact of nozzle diameter, number of nozzles, and different nozzle configuration on the cooling efficiency. Computational Fluid Dynamics (CFD) simulations were employed to analyze the maximum temperature, pressure drop, and the heat transfer characteristics at same flowrate condition and same impinging power condition. The results obtained from the simulations aided in determining the number of nozzles, their configuration, and the nozzle diameter that provided enhanced cooling effectiveness.

Building upon the findings of the preliminary study, the subsequent investigation involved real rectifier diode and updated bus bar to evaluate the cooling performance using the optimal design parameters determined earlier. For the final study, a nozzle size of 0.762 mm (0.03 in) diameter was chosen, corresponding to the minimum required spacing between the bus bar and the manifold.

Additionally, the bus bar was modified to ensure control over nozzle-to-target spacing. Numerical simulations were also performed at three different nozzle-to-target spacing.

The outcome of this research contributes to the understanding of jet cooling as an effective thermal management solution for complicated geometry bodies. The knowledge and insights gained from this study can guide future research efforts aimed at enhancing optimization of jet cooling systems to facilitate improved thermal management of rectifier diodes in aerospace.

Acknowledgment

I express my deep gratitude to my advisor, Dr. Stefan Moldovan for his invaluable mentorship and guidance to my academic development throughout the completion of this project. His feedbacks, expertise, and insight have been of great importance to me, and I am grateful for having him as my advisor.

I would also like to thank my committee members, Dr. Virgil Solomon, and Dr. Kyosung for their helpful feedback and suggestions. I am thankful for their willingness to take the time to read my work and offer their insights. Thanks to Mr. Eric Hakee for his technical assistance from time to time. His help was also essential to the completion of this project.

Beyond the academic realm, a special thanks to the Safran team for their insights and feedback on my work. I would also like to thank YBI team for providing manufacturing support.

To my beloved parents, Thakur Poudel and Durga Poudel, thank you for your unconditional love and belief in my abilities. Your sacrifice and unwavering support are the driving force behind my accomplishments. To my dear sisters, Samjhana, Archana, and Sujana. Finally, I am grateful to my friends, who have been with me through joys and sorrow, cheering me on and celebrating every small victory. I am so grateful for your friendship.

Contents

List of figures

List of tables

Nomenclature

d	nozzle diameter.
h	nozzle-to-target spacing.
R_{ij}	radius of circular hydraulic jump.
Re_d	Reynolds number based on diameter of nozzle.
g	acceleration due to gravity.
Q	flow rate.
ν	kinematic viscosity.
u_f	jet velocity.
D	diameter of target surface.
R	radius of the target surface.
$\overline{Nu}$	local average Nusselt number.
Nu_D	average Nusselt number on the target.
Nu_o	stagnation point Nusselt number on the target.
δ	viscous boundary layer thickness.

δ_t	thermal boundary layer thickness.
t	film thickness.
Pr	Prandtl number.
B	dimensionless velocity gradient.
U	heat transfer coefficient.
k	thermal conductivity.
IP	Impingement power.
IP^*	Dimensionless impinging power.
ρ	fluid density.

1. Introduction

A jet impinging cooling system consist of a focused stream of fluid released against a surface for increasing the effectiveness of heat transfer between the target surface and the fluid. It might consist of an array of jet arrangement in many applications. When fluid of same chemical composition and phase as the ambient fluid is aimed at the surface it is called submerged jet while jets having dissimilar characteristics are called free jets. Furthermore, impinging jets can be classified as unconfined and confined jets. Unconfined jets allow more interaction with the surrounding fluid as the jets are free to expand after they have struck the target surface while confined jets are bounded between two surfaces.

Jet impingement is utilized in a range of industrial and engineering applications as it provides an attractive mean to obtain large heat transfer coefficients on a solid target surface [1]. Some heat transfer applications include heat exchangers in automotive and aeronautical industry, drying of paper, cooling of turbine components, de-icing of optical surfaces, cooling of photovoltaic cells, etc. It is also used in drying and removal of small surface particulates in mass transfer applications [1].

With the recent development in electronic microchips or integrated circuits, a need for cooling technique has arisen that is capable of absorbing very high heat fluxes under compact hardware arrangements. Jet impingement cooling can be a very decent choice in this matter, however when developing such a cooling system the influence of jet velocity, fluid properties, jet dimensions, target surface dimension, the nozzle-to-surface spacing, etc. must be fully understood.

1.1 Research Objectives

Jet impinging can enhance cooling in the aerospace industry as the electrical systems are taking over hydraulic systems which has caused in rise of electrical power levels in all aircrafts [2]. Growing use of radar systems directed energy weapons (laser), electronic jamming, etc. also contribute to the growing demand of electrical power in aerospace. High Voltage DC generators can achieve higher power with less weight but there are significant challenges still present. One of those challenges includes heat generation in the rectifier module when converting AC to DC internally within the generator.

The goal of this project is designing a jet impinging cooling system for diodes used on rectifier modules. The objectives of the research include:

1. Design and manufacture a cooling system for rectifier diodes using jet impingement that can remove maximum amount of heat generated during the conversion of AC to DC power in a reliable, efficient, and cost-effective manner.
2. Numerical thermal modeling to analyze and quantify the performance of the cooling system and to determine the heat transfer coefficient on the target surface.
3. To perform parametric studies on the cooling efficiency using different nozzle sizes, flow rates, and nozzle-to-plate spacing and validate the numerical simulation with experimental results.
4. To provide new insights and findings in the field of impinging jet cooling and provide recommendations for their effective implementation.

2 Literature Review

Numerous studies have been done on the physics of impinging jets. The geometric parameters of most importance for an impinging jet analysis are nozzle diameter (d) and nozzle-to-plate spacing (h). Fluid properties such as density, viscosity and surface tension have also been part of the problem while studying an impinging jet.

When a high velocity liquid flow is slowing down to lower velocity, there is a rise in the fluid's film thickness. This sudden rise in thickness of the fluid is termed as hydraulic jump and can be seen in open channel flows like rivers and canals, and in industry and manufacturing processes. This phenomenon is mostly dependent on the initial speed of the fluid which implies that there is a critical speed at which hydraulic jump to appears [3].

2.1 Flow-Field

Liquid jets flowing perpendicular to a flat surface spread radially into a thin film which increases the heat transfer due to convection on the target surface. Watson [4] subdivided the jet impingement the jet impingement flow into four regions:

1. The stagnation region where the fluid impacts the solid surface directly.
2. The boundary layer region where the thickness of the viscous boundary layer is less than the thickness of the liquid sheet.
3. The fully viscous region where the thickness of boundary layer is same as liquid sheet thickness.

4. The hydraulic jump where the interaction between higher velocity fluid and lower velocity fluid results in an increase in the thickness of the fluid's film.

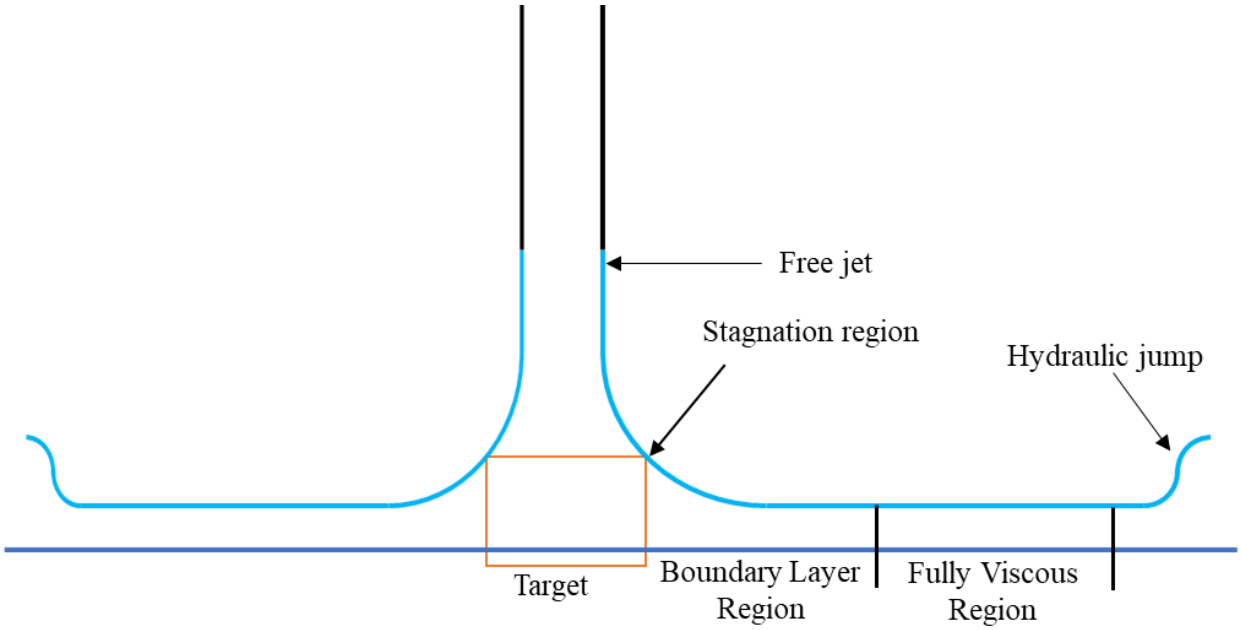

Figure 1: Jet impingement flow field regions.

He found a theoretical solution for the region 2 and region 3 by a similarity solution of the boundary layer equation which led to Blasius type similarity solution for the fully viscous region. He also noted that for velocity profile in the similarity solution for two-dimensional case is same as the in axisymmetric case. He applied inviscid theory to analyze the hydraulic jump.

Liu and Lienhard [5] investigated jet impinging heat transfer using uniform heat flux on the surface. They found that after exiting the nozzle, the jet spreads in a radial direction developing into viscous and thermal boundary layers while hydraulic jump or boiling might also occur depending upon the jet Reynold's number, temperature at nozzle exit, target's heat

flux, and fluid properties. Following the work of Watson [4], the authors subdivided radial flow of an impinging jet into four different regions: the stagnation zone, boundary layer zone, fully viscous sheet, and the hydraulic jump.

Baonga et al. [6] utilized nozzle diameters 2.2 mm and 4 mm to conduct their experiment and suggested a co-relation for hydraulic jump radius as a function jet's Reynolds number.

$$R_{ij}/d = 0.0061 Re_d^{0.82} \quad (1)$$

The jets Reynolds number was in the range 600 - 9,000 for their experiments. Above equation predicts the hydraulic jump radius with an error of 15% (average) compared to the experimental measurements done by Steven and Webbs [7] who suggested the following equation for the jump radius:

$$R_{ij}/d = 0.046 Re_d^{0.62} \quad (2)$$

The above equation predicted the radius or the location of hydraulic jump with 15% error without not including the influence of nozzle-to-plate spacing. To correlate nozzle-to-plate distance with the hydraulic jump, Brechet and Neda [8] studied the circular hydraulic jump both theoretically, and experimentally to propose an equation based on the flow rate, drop height, and fluids kinematic viscosity:

$$R_{hj} = \left(\frac{27 g^{-\frac{1}{4}}}{2^{\frac{1}{4}} 35\pi} \right) Q^{2/3} h^{-1/6} \nu^{-1/3} \quad (3)$$

However due to experimental scatter, they were not able to conclude the exact effect of nozzle-to-plate distance on the radius of hydraulic jump.

To understand the effect of nozzle diameter on the radius of circular hydraulic jump, Choo et al. [9] investigated seven different nozzle diameters (0.381-8mm). Interestingly, it was concluded that there was almost no effect of nozzle diameters on hydraulic jump under fixed impingement power condition however, under fixed jet Reynolds number the decrease in nozzle diameter increases the radius of the circular hydraulic jump. The pumping power is also an important constraint for an impinging jet problem as it has an effect on operating cost. They suggested the following equation for jump radius:

$$\frac{R_{ij}}{d} = \left[\frac{\pi}{8}\left(\frac{u_f^3 d^2}{\nu^{7/3} g^{1/3}}\right)\right]^{\frac{1}{4}} \quad 4$$

In the impingement region or the deflection zone a significant drop in axial velocity and an increase in static pressure was observed. Tani and Komatsu [10] performed a series of experiments on a low speed round circular jet to show that the deflection zone extends two nozzle diameters from the point of impingement on flat solid target surface. However, Giralt et al. [11] found the size of this region to be $1.2d$.

Several numerical simulations methods have been applied to model the hydraulic jump radius. For a laminar circular jet of radius 1.6 mm, Wang and Khayat [12] studied the impacts of gravity as well as surface tension on the circular hydraulic jump for highly viscous fluid called silicon oil and water. They concluded that due to strong hydrostatic pressure gradients in high viscosity fluid, gravity is the predominate factor in the occurrence of hydraulic jumps.

Whereas, for the low viscosity liquid (water), circular hydraulic jump was mainly induced by the influence of surface tension.

Raghav [13] studied impinging jet with water on a hot flat aluminum plate under turbulent condition with a constant nozzle-to-plate spacing and compared various CFD transient models of an impinging jet using ANSYS FLUENT. Using k-ε RNG model he was able to best correlate his work with the existing experiment, but the Nusselt number was overestimated. The axisymmetric liquid sheet thickness along the radial direction had good agreements with the work of [5]. Using the same turbulence model, Hosain [14], found similar results. The velocity profile with was in good with available literature however, the Nusselt number was not accurate although following similar trends.

K-ω turbulence model can be considered good alternative to Reynolds Stress Model (RSM) with a little compromise in the accuracy [1]. Also, low Reynolds k-ω model can produce promising results by matching the shape of the experimental geometry Zuckerman and Lior [1]. Balachandar et al [15] compared turbulence models such as k-ε Realizable, k-ω SST, and RSM. The centerline velocity profile was best estimated by k-ω SST for $h/d = 180.5$ and $Re_d = 100{,}000$ on comparison with the experimental work of Giralt et al. [16].

2.2 Heat Transfer

In 1965, Brdlik and Savin [17] recommended a correlation for submerged jet which was applicable for $h + R \leq 6.2d$, $h/d \leq 6.2$, $1.67 < D/d \leq 18.75$, and $2{,}000 < Re_d \leq 20{,}000$.

$$Nu_D = 10.54\, Re_D^{00.5} Pr^{0.33} \quad (5)$$

The characteristic length they chose here was the diameter of the plate that the jet was impinging on. Another correlation for local Nusselt number was suggested by Martin [18]. Range of validity: $2{,}000 \leq Re_d \leq 400{,}000$, $20.5 \leq R/d \leq 70.5$, and $2 \leq h/d \leq 12$.

$$\overline{Nu} = \left(\frac{d}{R}\right) \frac{1 - 1.1(d/R)}{1 + 0.1((h/d - 6)(d/R)}\, F(Re_d)\, Pr^{0.42} \quad (6)$$

Where,

$$F(Re_d) = 1.36 Re_d^{00.574}\ for\ 2{,}000 < Re_d < 30{,}000$$

$$F(Re_d) = 00.54 Re_d^{0.667}\ for\ 30{,}000 < Re_d < 120{,}000$$

$$F(Re_d) = 0.151 Re_d^{0.775}\ for\ 120{,}000 < Re_d < 400{,}000$$

With a smooth curve fitting $F(Re_d)$ can be better represented as:

$$F(Re_d) = 2\, Re_d^{00.5} \left(1 + \frac{Re_d}{200}\right)^{00.5} \quad (7)$$

Watson's [4] work was utilized by Chaudhary [19] to find the temperature profile along a wall with uniform temperature, at the locations where similarity solution of the momentum equation was available accounting the effects of viscous heating, initial heating, and wall heating condition separately.

Lienhard et al. [5] also sub-divided the heat transfer regions into six different regions and provide analytical solution for the region 2, 3 and 4 for liquids with $Pr > 1$.

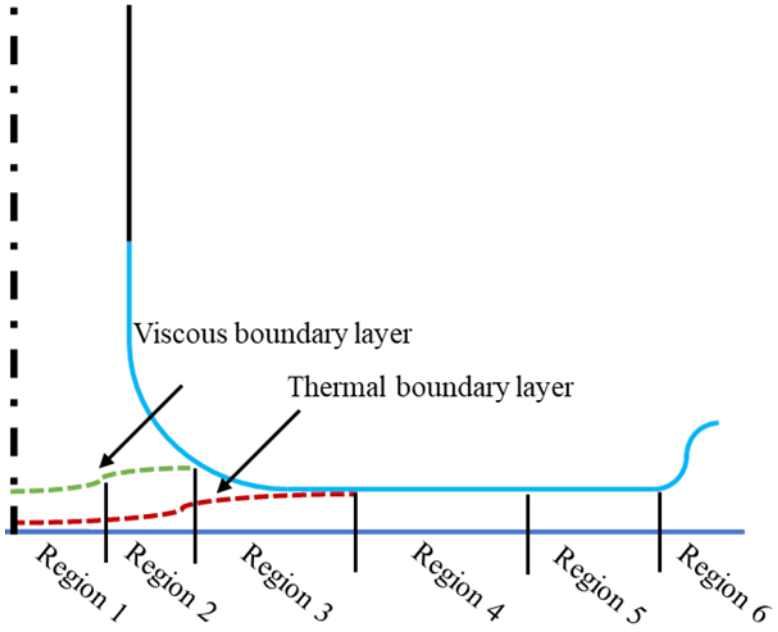

Figure 2: Jet impingement heat transfer regions

1. Region 1: The stagnation region.
2. Region 2: $\delta < t$ region: Outside of viscous the boundary layer, the velocity of the fluid is unaffected by the solid surface and is therefore equal to the fluid velocity exiting the jet.
3. Region 3: $\delta = t$ and $\delta_t < t$ region: The temperature of the fluid outside the thermal boundary layer remains unaffected by the heat transfer taking place at the solid surface.
4. Region 4: $\delta = t$ and $\delta_t = t$ region: The thermal boundary layer extends up to the surface of the liquid sheet.
5. Region 5: This region might include nucleate boiling, burnout, and dry surface in the presence of sufficiently high heat flux.
6. Region 6: The hydraulic jump.

In region 2, the local Nu number was given as:

$$Nu_R = 0.632 Re_d^{0.5} Pr^{\frac{1}{3}} \left(\frac{R}{d}\right)^{0.5} \quad 8$$

When $R = R_o = 0.1773\, Re_d^{\frac{1}{2}}\, d$, region 2 end and region 3 begins. In region 3 the local Nusselt number was determined to be:

$$Nu_R = \frac{0.407\, Re_d^{\frac{1}{3}}\, Pr^{\frac{1}{3}}\, \left(\frac{d}{R}\right)^{\frac{2}{3}}}{\left[0.1713 \left(\frac{d}{R}\right)^2 + \frac{5.147R}{Re_d d}\right]^{\frac{2}{3}} \left[\frac{1}{2}\left(\frac{R}{d}\right)^2 + C_3\right]^{\frac{1}{3}}} \quad 9$$

Here, the constant C_3 is a constant of integration given by:

$$C_3 = \frac{0.267\ \left(\frac{d}{R_o}\right)^{\frac{1}{2}}}{\left[0.1713 \left(\frac{d}{R_o}\right)^2 + \frac{5.147R_o}{Re_d d}\right]^2} - \frac{1}{2}\left(\frac{R_o}{d}\right)^2$$

For region 4,

$$Nu_R = \frac{0.25}{\frac{1}{PrRe_d}\left(1 - \frac{R_1^2}{R^2}\right)\left(\frac{R}{d}\right)^2 + 0.130\frac{h}{d} + 0.0371\frac{t_{R_1}}{d}} \quad 10$$

Region 4 starts at $R = R_1$ which is defined as:

$$\left(\frac{R_1}{d}\right)^3 + p\left(\frac{R_1}{d}\right) + s = 0$$

$$p = \frac{-2C_3}{(0.2058\,Pr - 1)}$$

$$s = \frac{0.00686 Re_d Pr}{(0.2058\,Pr - 1)}$$

It was also pointed out that, region 4 only occurs at critical Prandtl number, $Pr < 4.859$.

Extensive experiments have been done characterized to Nusselt number for an impinging jet. Stevens and Webb [7] expected the stagnation zone to extend up to a dimensionless distance of $R/d \leq 0.75$ and quantified the local heat transfer coefficient at stagnation for jet impinging with a round nozzle on a surface with uniform heat flux solid surface. They were able to propose a correlation for the stagnation point Nusselt number which was able to predict the experimental outcomes with a maximum error ranging from 5 to 14 percent across all nozzle sizes tested in the experiment. The suggested co-relation is that follows:

$$Nu_o = 2.67 Re_d^{00.567} Pr^{0.4} \left(\frac{h}{d}\right)^{-0.0336} \left(\frac{u_f}{d}\right)^{-0.237} \quad 11$$

Above equation is valid for $4{,}000 < Re_d < 52{,}000$. It can be noticed that the nozzle-to-plate spacing has least influence on the stagnation point Nusselt number. Based on this correlation another correlation for local Nusselt number along the surface was also proposed by [7].

$$\frac{Nu(R)}{Nu_o} = \left[1 + \left(aexp\left(b\left(\frac{R}{d}\right)\right)\right)^{-9}\right]^{-0.11} \quad 12$$

Equation (11) has been found to be sensitive of nozzle sizes. For same Reynolds number, difference up to 40% has been observed on the local Nusselt number [20], as for turbulent jets the mean radial velocity gradient had more influence in determining the Nusselt number. So, incorporating the dimension less velocity gradient in the [20] suggested the following co-relation for the stagnation region Nusselt number.

$$Nu_o = 0.69(BRe_d)^{0.5}Pr^{0.4} \quad 13$$

It was also mentioned that equation (13) should not be used in thermal design of impinging jets without the proper understanding of hydrodynamic condition at the stagnation region.

The dependency of nozzle-to-plate on fluid flow and heat transfer for a range of spacing ($h/d = 0.1 - 40$) were investigated by Choo et al. [21]. They divided the range of nozzle-to-target spacing into jet deflection region for $h/d \leq 0.6$, potential core region extending from $0.6 < h/d \leq 7$, and free jet region from $7 < h/d \leq 40$. In jet deflection, the normalized stagnation Nusselt number increases as the h/d decreases. In potential core however, minimal effect h/d on the stagnation Nusselt number was observed and in the free jet zone, monotonical decreases in the normalized stagnation Nusselt number with the increase in h/d was seen during the experiment. They proposed a relation for stagnation Nusselt number solely in terms of h/d:

$$Nu_0^* = \sqrt{4\exp(-(h/d)/0.14) + \left\{00.57 - 00.5tanh\left(\frac{(h/d) - 15}{11}\right)\right\}} \quad 14$$

Experimental results of Baughn and Shimizu [22] showed that at $h/d = 6$ heat transfer occurs at its maximum at the stagnation point. Also, at $h/d = 2$, maximum heat transfer occurs at stagnation point followed by other maxima at $R/d = 1.8$. The heat transfer has a minimum value at the dimensionless distance of $R/d = 1.3$.

Significant progress has been made in numerical modeling of heat transfer as well as flow for an impinging jet. Till date the best performing turbulence model for impinging jet application is V2F model (normal velocity relaxation model). This model aims to capture both the near-wall and free-stream turbulence characteristics by incorporating turbulent stress which is normal to the streamlines and referred as $\overline{v^2}$, to find turbulent eddy viscosity i.e., $v_t = C_\mu \overline{v^2} T . \overline{v^2}$.

For a constant $Re_d = 23,000$ $(0.5 \leq h/d \leq 14)$, Behnia et al. [23] investigated the effectiveness of V2F model and $k - \varepsilon$ model in predicting the heat transfer and flow field characteristics. Their results were consistent with the findings of [22] when using V2F model. It was found that $k - \varepsilon$ model (which uses k to determine the turbulent viscosity) over-predicted the stagnation Nusselt number and flow characteristics. This flaw was due to $k - \varepsilon$ model overpredicting turbulent kinetic energy 80% higher than V2F which instead should be low. Similar results were found by same sets of researchers [24] when studying confined and unconfined jets who reported $k - \varepsilon$ producing excessive turbulence.

Balachandar et al. [25] were able validate their results, using SST $k-\omega$ turbulence model, with co-relation provided by [7] with error of 30.5, 5, and 8 for respective nozzle sizes of 1, 2 and 4 mm. In addition to turbulence modeling, they utilized Volume of Fluid (VOF) multiphase model to capture the interface between the fluids (air and oil). The paper suggest that larger nozzle size produce more uniform temperature distribution (in other words, more uniform cooling was observed with larger nozzle) while smaller nozzle produce more efficient cooling at the stagnation zone. Based on the results from their simulation they provided following co-relation for stagnation Nusselt number.

$$Nu_o = 0.0142 {Re_d}^{0.565} Pr^{0.4} B^{3.41} \quad (15)$$

In equation (15), the quantity B is based on the analytical solution provided by [26] and was calculated using equation (16). This approach relies on inviscid or laminar theory and does not incorporate a well-established method for evaluating the radial velocity gradient in turbulent jets. Consequently, the effects of turbulence were not accounted for.

$$B = 2\left(\frac{d}{u_f}\right)\left(\frac{du_r}{dR}\right) \quad (16)$$

And the velocity gradient at the stagnation zone was evaluated as:

$$\left(\frac{dv_r}{dR}\right) = 1.9\left(\frac{v_f}{d}\right)^{0.95} \quad (17)$$

3 Governing Equations

3.1.1 Turbulence model equation

The commercial ANSYS FLUENT solves the conservation of mass and momentum equation for any given flow. For turbulent flows another set of transport equations are introduced to the equations. For laminar flows, equation of mass conservation for both compressible and incompressible fluid is given as:

$$\frac{\partial \rho}{\partial t} + \nabla.(\rho \vec{v}) = S_m \tag{18}$$

S_m represents the mass source term from any user defined source and mass source included to the continuous phase from the dispersed phase. The momentum equation used in FLUENT is described by following equation:

$$\frac{\partial}{\partial t}(\rho \vec{v}) + \nabla.(\rho \vec{v}\vec{v}) = -\nabla p + \nabla.(\bar{\bar{\tau}}) + \rho \vec{g} + \vec{F} \tag{19}$$

Where, p is the static pressure, $\bar{\bar{\tau}}$ represents the stress tensor, $\rho \vec{g}$ is the gravitational body force and $\vec{F}$ is the external body force. The form of $\bar{\bar{\tau}}$ is given below:

$$\bar{\bar{\tau}} = \mu \left[\nabla.\vec{v} + \nabla.\vec{v}^T - \frac{2}{3} \nabla.\vec{v} I \right] \tag{20}$$

Here, I and $\nabla.\vec{v}^T$ represent the unit tensor and effect of volume dilation respectively.

ANSYS FLUENT has various turbulence model listed for different applications. For impinging jets application most of literature [1] [24] [27] [28] suggest $v^2 - f$ model, this

model has been discontinued by ANSYS FLUENT. Thus, $k-\omega$ SST was picked for the current simulation. The transport equations for $k-\omega$ SST model is given below:

$$\frac{\partial}{\partial x}(\rho k)+\frac{\partial}{\partial x_i}(\rho k u_i)=\frac{\partial}{\partial x_j}\left(\Gamma_k\frac{\partial k}{\partial x_j}\right)+G_k-Y_k+S_k \quad (21)$$

$$\frac{\partial}{\partial t}(\rho\omega)+\frac{\partial}{\partial x_i}(\rho\omega u_i)=\frac{\partial}{\partial x_j}\left(\Gamma_\omega\frac{\partial \omega}{\partial x_j}\right)+G_\omega-Y_\omega+D_\omega+S_\omega \quad (22)$$

The term G_k is production of turbulent kinetic energy due to the mean velocity gradient, G_ω is the generation of ω and are given as:

$$G_k=-\rho u_i' u_j'\frac{\partial u_j}{\partial x_i}$$

$$G_\omega=\alpha\frac{\omega}{k}G_k$$

S_k and S_ω are the user defined source term. Further details of the of these equation, terms, and modeling can be found in FLUENT Theory Guide and User Manual [29].

3.1.2 Heat Transfer equations

To model the thermal effects, FLUENT adds the energy equation in the computation. The energy conservation in fluids and solids is solved using separate equations in FLUENT. For fluids,

$$\frac{\partial}{\partial x}(\rho E)+\nabla.(\vec{v}(\rho E+p))=\nabla.\left(k_{eff}\nabla T-\sum_j h_j\vec{J}_j+\left(\vec{\tau}_{eff}\vec{v}\right)\right)+S_h \quad (23)$$

k_{eff}=effective conductivity

$\vec{J}_j$=diffusion flux of species *j*

$k_{eff}\ \nabla T$=energy transfer due to conduction.

$\sum_j h_j \vec{J}_j$=species diffusion

$\vec{\tau}_{eff}\vec{v}$=viscous dissipation

S_h= volumetric heat source.

$$E = h - \frac{p}{\rho} + \frac{v^2}{2}$$

h is the enthalpy defined as:

$$h = \sum_j Y_j h_j + \frac{p}{\rho}$$

The mass fraction of species j is represented by the term, Y_j and h_j is given as follows:

$$h_j = \int_{T_{ref}}^{T} C_{p,j} dT$$

The reference temperature, T_{ref}=298.15K.

For solids, the energy equation is given as:

$$\frac{\partial}{\partial x}(\rho h) + \nabla.(\vec{v}\rho h) = \nabla.(k\nabla T) + S_h \quad (24)$$

The terms $\nabla.(\vec{v}\rho h)$ and $\nabla.(k\nabla T)$ are the convective energy transfer due to the motion of the solids and heat flux due to conduction in the solids respectively.

The conductive heat transfer coefficient from the heat flux at the wall is calculated using equation (25).

$$q'' = U(T_s - T_{ref}) \quad (25)$$

T_s and T_{ref} are the temperature of the wall surface and fluid inlet temperature respectively. From the Fourier law of heat conduction, the heat flux can be found using.

$$q'' = -k\frac{\partial T}{\partial y} \quad (26)$$

The Nusselt number is based on the heat transfer coefficient, nozzle diameter, and the thermal conductivity and given as follows:

$$Nu = \frac{Ud}{k} \quad (27)$$

3.1.3 Multiphase model equation

There are mainly four types of multiphase phenomena that are encountered in nature and technology: the three phase flows, liquid-solid flows, gas-liquid or liquid-flow, and gas-solid flows. The first step to analyze multiphase flow is to determine the flow regimes.

Commercial ANSYS FLUENT provides three distinct Euler-Euler multiphase models available: the mixture model, the Volume of Fluid (VOF) model, and the Eulerian model.

VOF model was used in this work as it evaluates the volume fraction of fluid in all control volumes which is generally used for time dependent solutions, but it is sensible to use VOF model for steady-state solutions [29]. VOF model application includes predicting jet breakup, analyzing the motion of large bubbles in a liquid, studying the behavior of liquid after a dam break, and tracking the steady or transient motion of any liquid-gas interface [29]. Volume of Fluid model solves the following equation to track the interface(s) between any given phases.

$$\frac{1}{\rho_q}\left[\frac{\partial}{\partial x}\left(\alpha_q \rho_q\right) + \nabla.\left(\alpha_q \rho_q \vec{v}_q\right) = S_{\alpha_q} + \sum_{p=1}^{n} \dot{m}_{pq} - \dot{m}_{qp}\right] \quad 28$$

Where, $\dot{m}_{pq}$ represents the transfer of mass between phase q to phase p. The source term S_{α_q} is set to zero by default, however a user-defined or a constant mass source term can be defined in FLUENT. The above equation is for qth phase (secondary phase), VOF equation does not solve for the pth phase, instead it uses following constraint to evaluate the volume fraction of primary phase.

$$\sum_{q=1}^{n} \alpha_q = 1$$

VOF equation can either be solve implicitly or explicitly, however with explicit scheme a time dependent solution has to be exercised. For the current simulation, implicit

formulation was used as steady-state solutions were required. The implicit VOF equation solves the following equation which requires the volume fractions at current time step:

$$\frac{\alpha_q^{n+1}\rho_q^{n+1} - \alpha_q^n \rho_q^n}{\Delta t} + \sum_f \alpha_{q,f}^{n+1}\rho_q^{n+1} U_f^{n+1} = \left[S_{\alpha_q} + \sum_{p=1}^{n} \dot{m}_{pq} - \dot{m}_{qp} \right] V \qquad 29$$

Along with this compressive interface tracking scheme was used for the solution method. This is a high-resolution differencing scheme, suitable particularly for flows where the viscosities of the phases differ significantly [29].

3.1.4 Dimensionless impinging power

When a jet of fluid, strikes a surface, it transfers a certain amount of energy to that surface. This energy transfer can be quantified over time as power, which represents the rate at which energy is transferred. The impinging power is a measure of how much power is being transferred from the jet to the surface per unit of time. Impinging power can be calculated using following equation [9]:

$$I_p = \Delta P Q \qquad 30$$

Where, ΔP is difference in pressure between inlet and the impinging point or the stagnation point which can be evaluated using Bernoulli's equation and Q is the fluid flowrate, given as

$$\Delta P = \frac{1}{2}\rho u_f^2 \qquad 31$$

$$Q = \frac{\pi}{4} u_f d^2 \tag{32}$$

The factor used to non-dimensionalize the impinging power is given below:

$$f = \frac{\rho^{\frac{4}{3}}}{\mu^{\frac{7}{3}} g^{\frac{1}{3}}} \tag{33}$$

The units of f factor is $\frac{sec}{Joules}$, which is the reciprocal of units of watts, which is what the impinging power is measured in. Thus, the dimensional impinging power is given as:

$$IP^* = f \times IP \tag{34}$$

Impinging power is an important constraint while studying impinging jets as it is directly related to the cooling performance of the jets and the cost of operation. Researchers often take impinging power under consideration while studying impinging jets [9] [30].

4 Computational Methodology

4.1 Geometries

In this section, discusses the detailed geometry and dimensions of all the components that have been utilized in the analysis. This includes information on their cross-sectional profiles, shapes such as circular, rectangular, or any other specific geometrical configuration related to the study. Moreover, the section highlights any significant differences between the geometries that were used for the preliminary study and final study.

4.1.1 Rectifier diodes

There were two types of rectifier diode geometries used in the analysis. The left pair of images in Figure 3 depicts the actual geometry of the diode, while the right pair represents idealized diodes used for preliminary studies. The color coding applied to each picture follows a specific pattern: in each pair of pictures, the first picture is color coded based on the components, while the second picture is color coded based on the materials used.

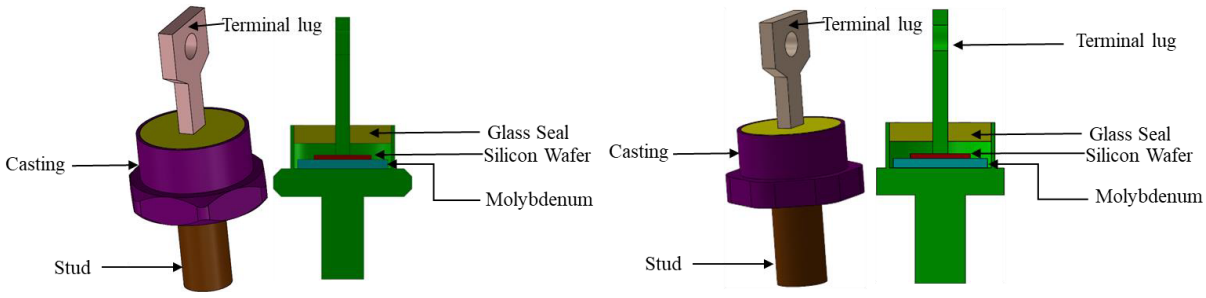

Figure 3: Rectifier Diode real geometry (left) and simplified geometry (right)

The major differences between diodes revolve around the outer casting. In the simplified model, the diode featured flat faces, whereas the actual diode had curved faces on the outer casting, as illustrated in Figure 4. Transitioning from the simplified to the real diode, both the height and length of the outer casting increased. Furthermore, the fillets at the corners of the hexagonal part in the real diode was half the size of the ideal diode. This difference resulted in the target face of the real diode being approximately 2.71 mm longer than that of the simplified diode.

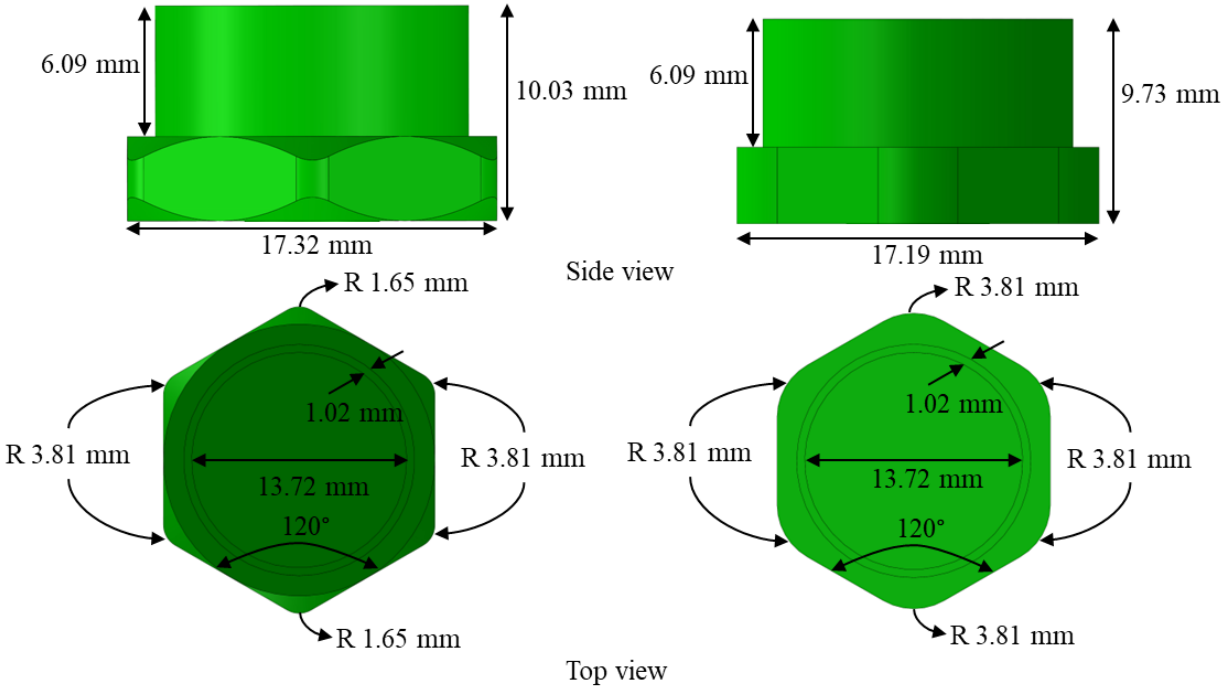

Figure 4: Outer casting real diode (left) and simplified diode (right)

Another distinguishing factor among the diodes lay in the varying shapes of their target faces as shown in Figure 5. The maximum height of the target surface increased by 0.3 mm in the real diode compared to the ideal diode. Slight change in the width and length of the

stud can also be noticed. Additionally, the total surface area of the real diode target face measured 27.23 mm^2, which was 26% larger than that of the ideal diode.

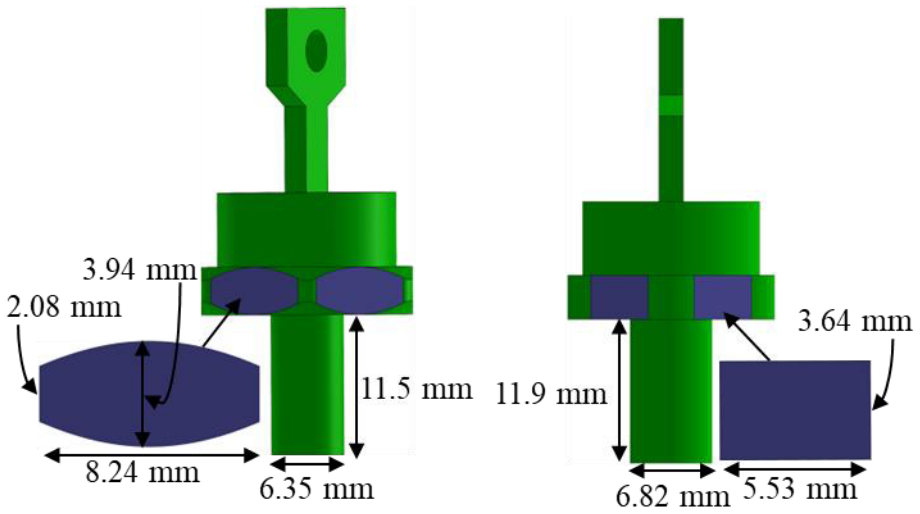

Figure 5: Comparison between target faces of real (right) and ideal (left) diode.

Additional components inside the diode casting include glass seal, silicon wafer, and molybdenum which remained unchanged along with the terminal lug, shown in Figure 6 in respective manner from left to right.

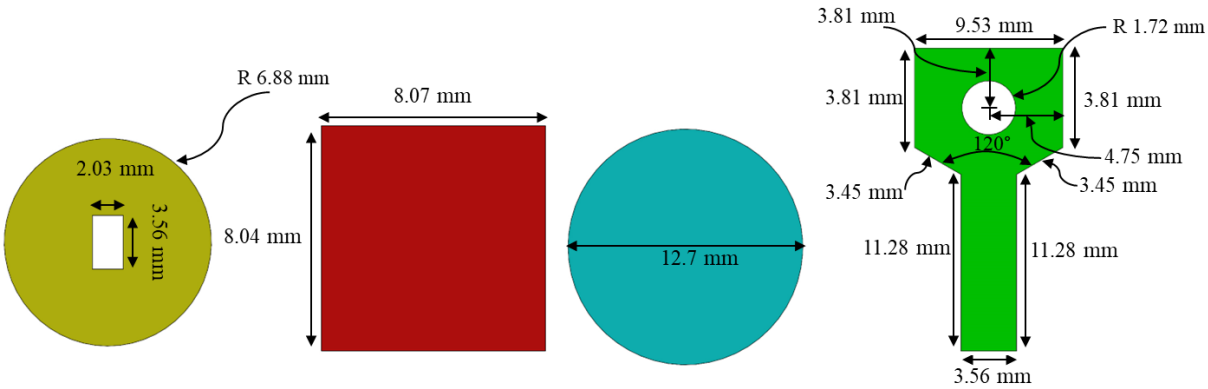

Figure 6: Unchanged components in real and simplified diode

The glass seal and molybdenum components had a round shape, with a thickness of 20.52 mm and 1.27 mm, respectively. The silicon semiconductor, on the other hand, had a thickness of 0.64 mm and a rectangular shape. Lastly, the terminal lug, serving as a connection point for external electrical circuitry, had a thickness of 2.03 mm.

4.1.2 Copper Bus Bar

For the study, two distinct copper bus bars were tested. The preliminary bus bar, depicted in Figure 7 was used for the 2 mm and 0.5 mm nozzle diameter geometries while the final bus bar, Figure 8 was designed for 0.762 mm nozzle diameter geometry.

4.1.2.1 Preliminary Bus Bar

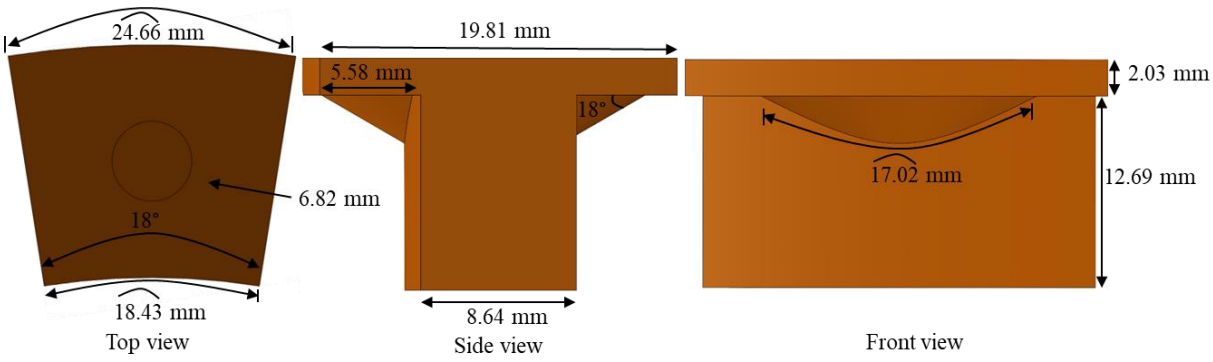

Figure 7:Copper Bus bar 1

Figure 7 shows the first initial design of the copper bus bar that was proposed. It was a T-shaped heat sink with two bumps on each side. The bumps were made to aid the heat transfer from the angled nozzle. The mass of initial copper bus bar was 22.41 grams.

4.1.2.2 Final Bus Bar

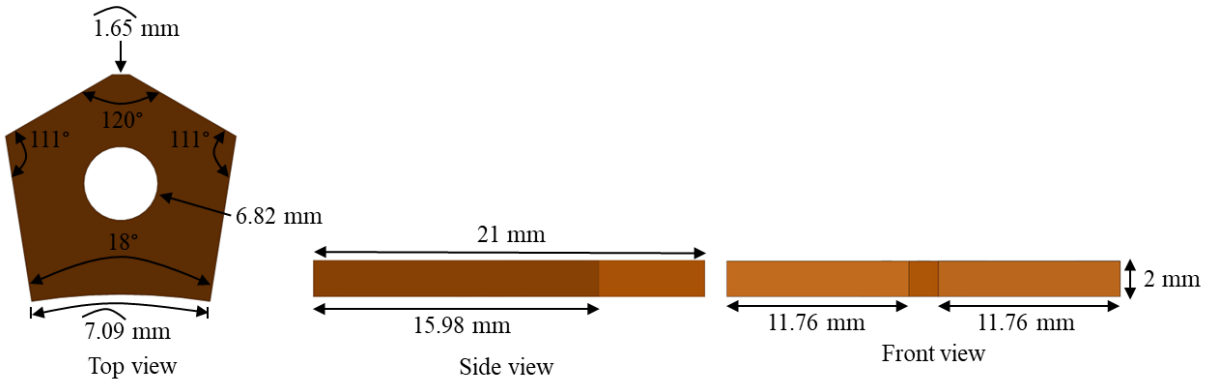

Figure 8: Final bus bar

The final copper bus bar was modified such that the weight was reduced by a factor of 3.7 (5.94 grams). As significant heat transfer was expected to occur only at the diode target, the T-section was removed for the finalized design.

4.1.3 Preliminary CFD Geometries

The computational geometry for the preliminary model is shown in Figure 9. It consisted of two nozzles targeting the diode faces while the third nozzle was aimed at the bumped section of the copper bus bar. The distance between the nozzles and their targets were maintained at 5 mm. The only difference between the two models lie in the size of the nozzle.

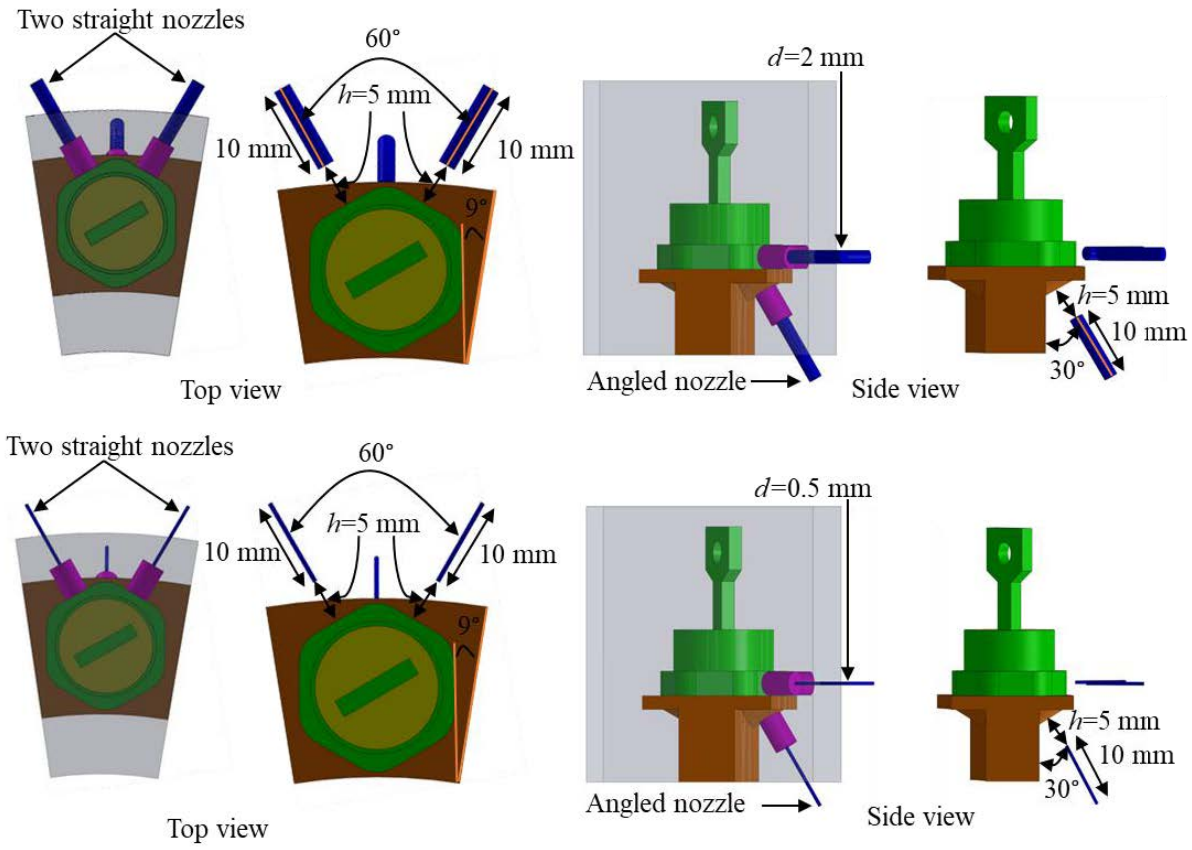

Figure 9:Preliminary geometries with 2 mm nozzles (left) and 00.5 mm nozzles (right)

The orientation of the diode was crucial in the analysis. Specifically, the diode was rested on the bus bar in a manner that ensured the straight nozzles, arriving at a 60° angle, would impinge upon the center of the target surface. To achieve this alignment, an angle of 9° was imposed between one of the diode's faces and the outer face of the bus bar. The round bodies shown in purple are the body of influences that allowed having a denser mesh near the target region of the diodes. These bodies of influences were made 30.5 mm in diameter and extended from the exit of the nozzle to the target surfaces.

4.1.4 Final CFD Geometry

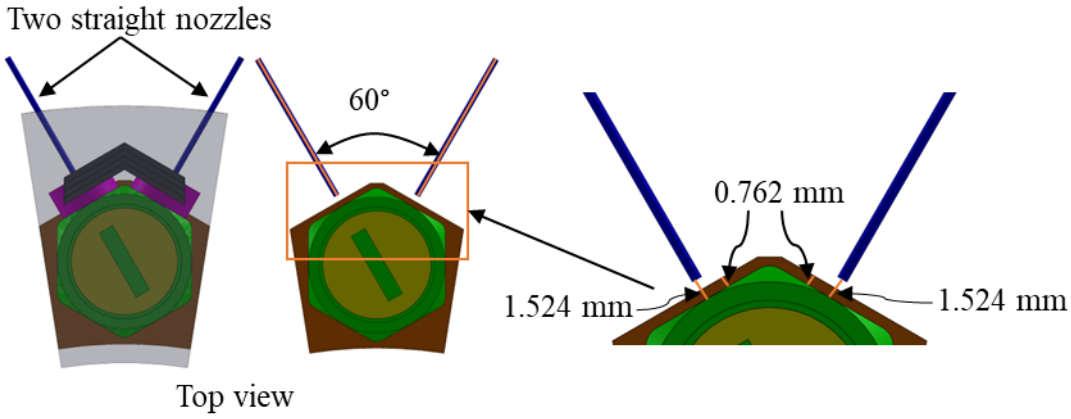

Figure 10:Final geometry top view

The final CFD model comprised of two straight nozzles coming at 60° towards the diode. The target faces of the diode were aligned parallel to the faces of the bus bar, both of which were facing the jet flow. This alignment was done to maintain the same orientation of the diode as in the preliminary geometry. Furthermore, a separation distance of one nozzle diameter was maintained between those two faces. The body of influences here were 10 times the nozzle diameter.

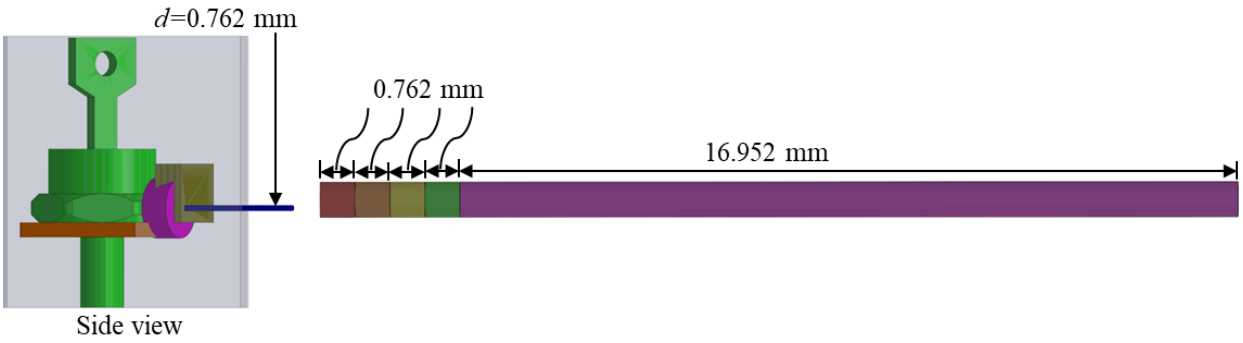

Figure 11: Final geometry side view

As shown in Figure 11, the nozzle was made in such a way that it allowed variable spacing between the jet and the target surface so that analysis at different nozzle-to-plate spacing could be performed. The walls of the manifold were also modeled for the final CFD geometry to test its effects on the heat transfer. The dimensions of the manifold walls are as follows:

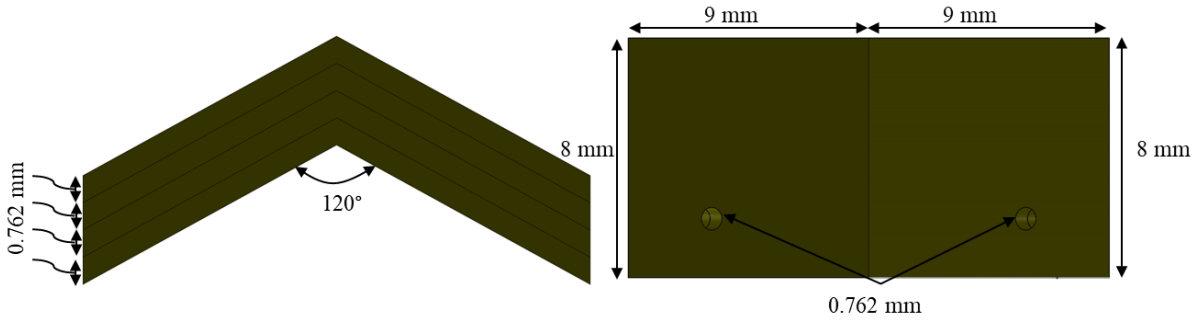

Figure 12: Manifold walls for 0.762 mm nozzle geometry.

4.2 Mesh

After completing the modeling of the CFD domains, the geometries were transferred to Design Modeler available in ANSYS Workbench package, where the naming convention was established. To generate meshes, ANSYS FLUENT Meshing was employed, utilizing a watertight geometry approach. By appropriately assigning names to prominent surfaces and bodies, FLUENT Meshing facilitates local sizing to specific regions. The resulting meshes were refined to ensure accurate representation and resolution of the desired flow and thermal features.

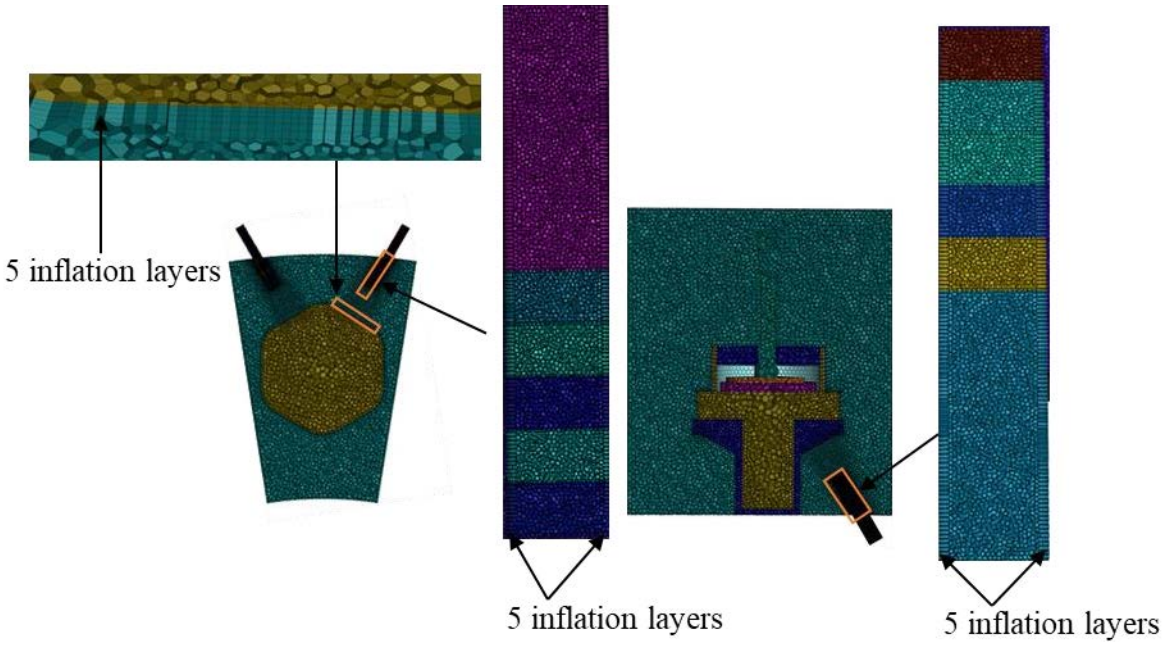

Figure 13: Mesh for 2 mm nozzle geometry

A consistent method was employed in meshing all three CFD geometries, involving the implementation of smaller mesh elements within the nozzle and around the target faces. To maintain consistency, certain mesh parameters were kept constant for the tested meshes. This included the first layer height, orthogonality, and the shape of the elements (polyhedral).

Inflation layers were employed within the nozzle walls and at the target surfaces to accurately capture the heat transfer and flow field in the boundary layer.

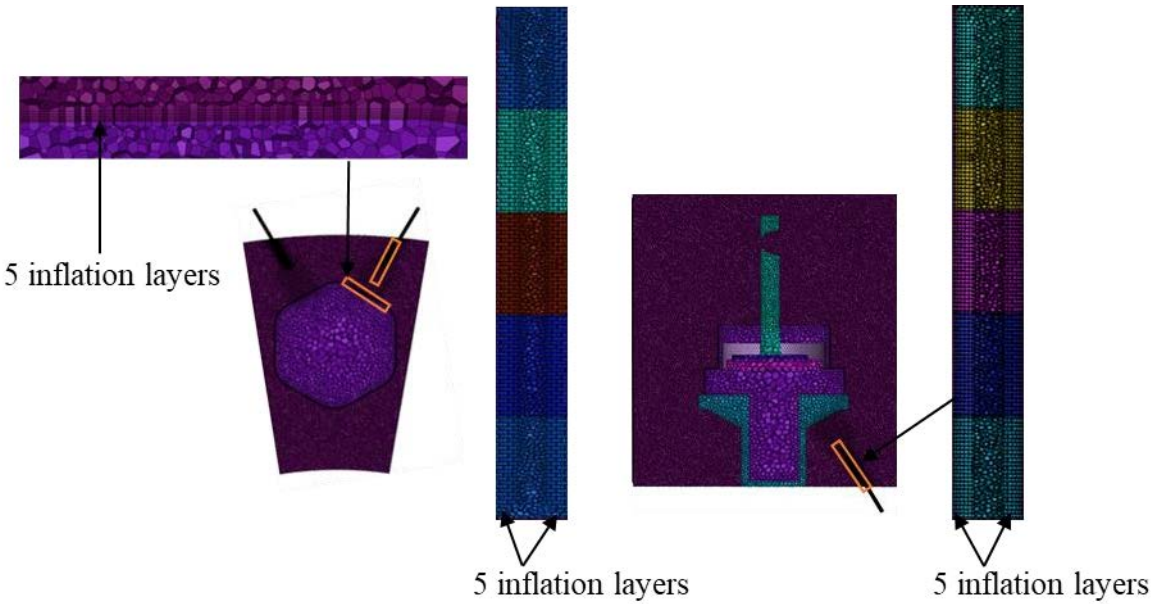

Figure 14:Mesh for 00.5 mm nozzle geometry

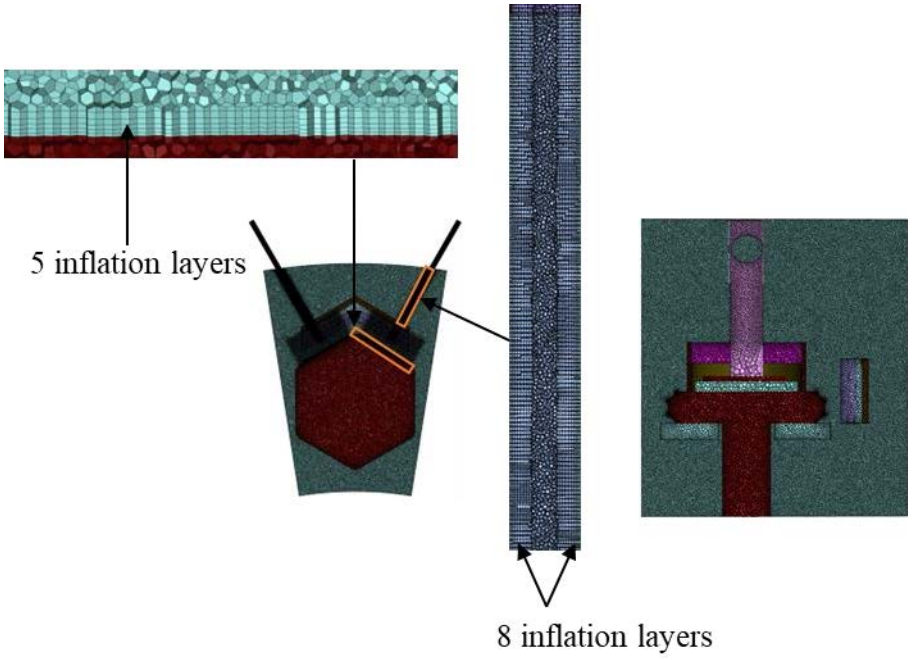

Figure 15: Mesh for 0.762 mm geometry

The critical meshing parameters are listed in Table 4-1

Table 4-1: Mesh parameters

	2 mm nozzle	0.5 mm nozzle	0.762 mm nozzle
No. of elements	1,580,298	2,981,860	5,667,567
First Layer Height [mm]	0.02	0.02	0.02
Orthogonality	0.2	0.2	0.2

4.3 Boundary Conditions

The boundary conditions were carefully defined and applied consistently across all the models.

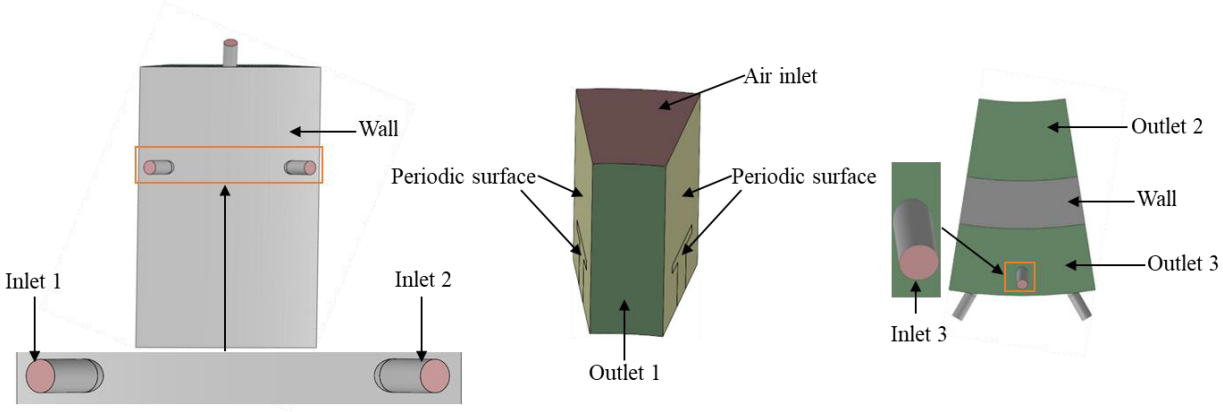

Figure 16: Boundary conditions on 2mm nozzle geometry

A unique boundary condition that was applied at the side surfaces was periodic boundary condition. When the expected flow, thermal solution, and the physical geometry exhibit a repeating nature periodically, this boundary conditions is employed [29]. With this approach, the simulation of smaller representative domain can be used to capture the periodic behavior which reduces the computational requirement. The reason for using periodic boundary conditions in the models is that in an aerospace generator there would be multiple diodes that need cooling at the same time.

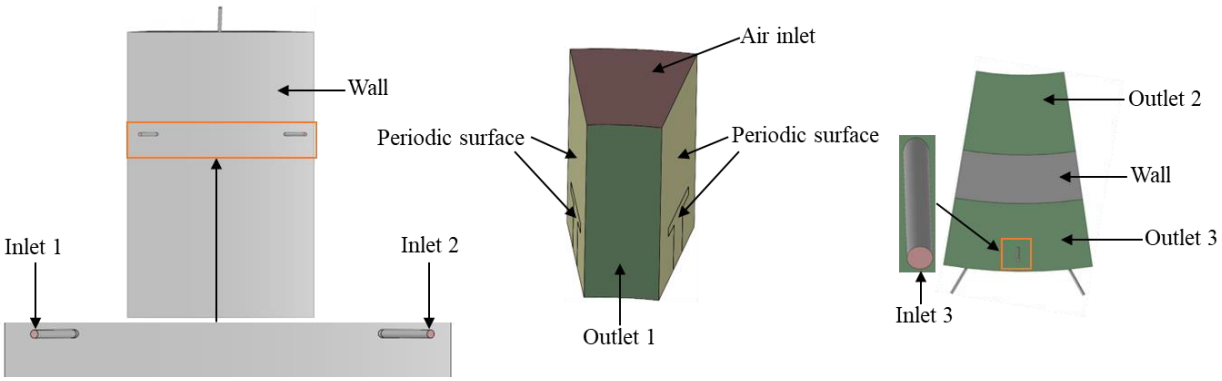

Figure 17: Boundary Conditions on 0.5 mm nozzle geometry.

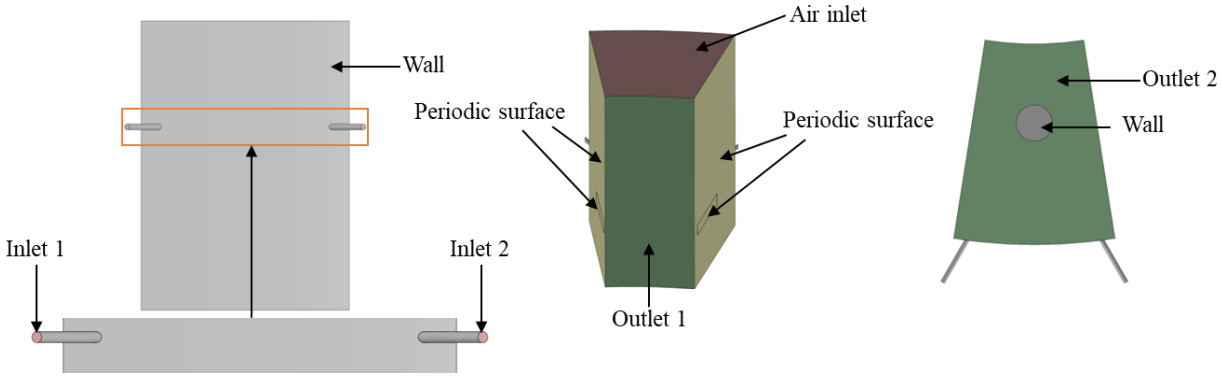

Figure 18: Boundary Conditions on 0.762 mm nozzle geometry.

In the preliminary models, four inlets and three outlets were incorporated, while the final model was modified to have three inlets and two outlets. The top section of the computational domain was set-up as an air inlet though ambient air was entering the domain at a low velocity of 0.1 m/s. The inlet air temperature was set at 150°C while the jets entering the domain had an inlet temperature of 135°C. These inlet conditions were choosen to closely replicate the thermal environment encountered in aerospace generators along with a turbulent intensity of 5% imposed at the inlet.

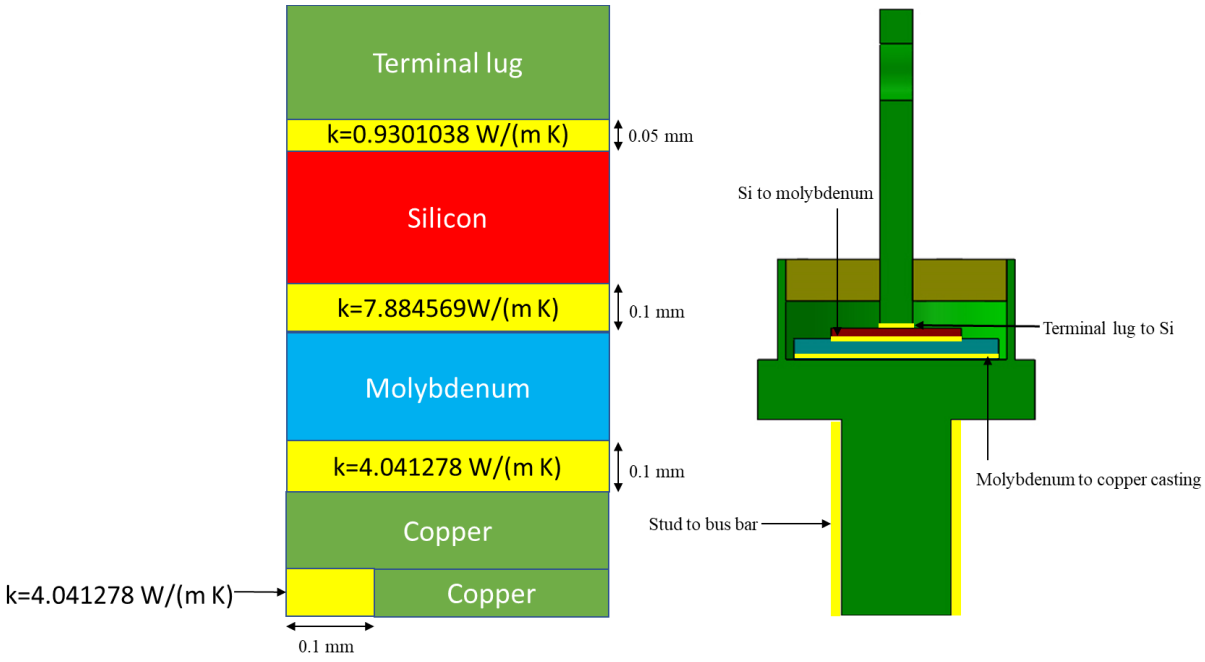

Figure 19: Thermal Contact Surfaces

Figure 19 shows the contact resistance that were applied at various contacts between diode's components. During the examination of the cross-section diode, it was observed that the terminal log and Si wafer exhibited a perfect contact and were effectively soldered together. Therefore, the contact thickness between these two components was approximately half the size of other contact materials. The soldering material employed for silicon, such as S-bond 220M, had a thermal conductivity of approximately 48 W/ (m K) [31]. Nevertheless, factors such as microcracks, intermetallic layers, and the crystal grain morphology at the solder-substrate interface affect the thermal conductivity, resulting in the solder joint's thermal conductivity being only around 14% of the expected value [32]. Based on these findings the thermal conductivity of terminal lug-Si contact material was set up in FLUENT.

A thermal load of 51 W was applied to the silicon wafer, serving as a heat source within the system. This heat is then transferred through thermal conduction to all other components, including the diode casting, the copper bus bar, and the jet target surface. Thus, the heat source is acting as a remote heat source for the jet target surface. Additionally, the jets are aimed horizontally towards the target surface which is different than most literature on jet impingement cooling [7] [25].

4.3.1 Material Properties

The oil used for cooling is aerospace Mobil Jet Oil 254. The material properties of the oil were variable with temperature. They were either a polynomial or a piecewise polynomial function of the temperature. The material properties are as follows:

- Density

$$\rho = -0.7231089 \times \mathrm{T} + 1210.454 \quad (35)$$

- Thermal Conductivity

$$k = 0.000318049 \times \mathrm{T} + 0.09434249 \quad (36)$$

- Specific Heat

$$C_p = \text{-}0.000122087 + \times \mathrm{T}^3 + 0.1342287 \times \mathrm{T}^2 \text{-} 45.04763 \times \mathrm{T} + 6583.77 \quad (37)$$

- Dynamic Viscosity

  Range 1 (311K - 422K)

$$\mu = 1.88879e-10 \times T^4 - 3.18417e-07 \times T^3 + 0.000200614 \times T^2 - 0.0560492T + 5.868354 \quad (38)$$

  Range 2 (422K - 500K)

$$\mu = -1.89368e-05 \times T + 0.01025524 \quad (39)$$

5 Results

To better show the interactions between the two phases (oil and air) in the flow and the solid bodies two cross section planes were created. One is a horizontal cross section through the center of the nozzle. The other is a vertical cross section through the center of the diode in the radial direction. The contours presented in the following sections are from the cross-sections shown in Figure 20 and Figure 21.

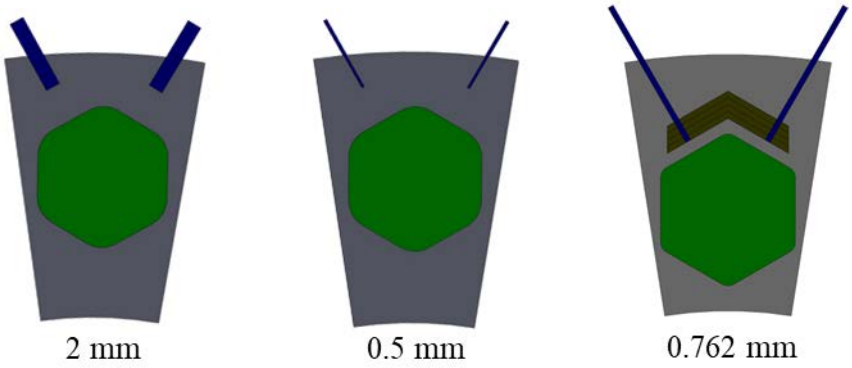

Figure 20: Cross-section 1.

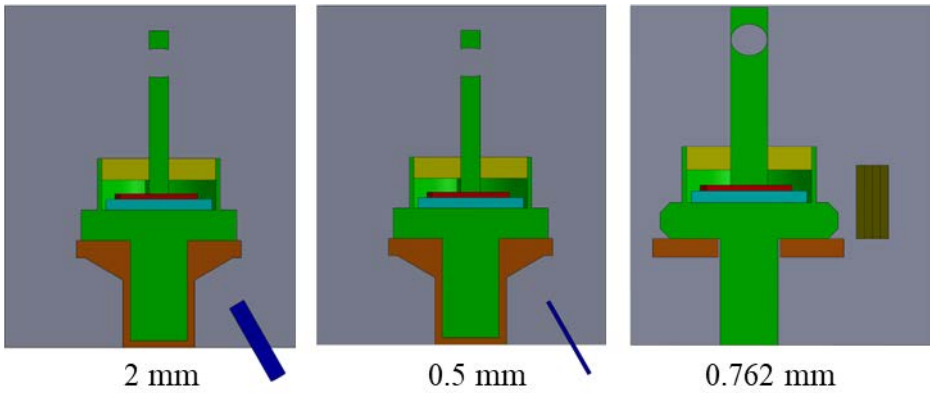

Figure 21: Cross-Section 2.

5.1 Grid Convergence Test

Grid Convergence was performed for the final model at 1 GPM flowrate. The results are listed below:

Table 5-1:Results from Grid Convergence.

Grid Size	Max Si Wafer Temp [°C]	% Difference
358,351	174.40	9.18%
2,868,762	177.03	3.12%
5,667,567	178.38	Baseline

The % difference in temperature between two grid size was calculated using equation 40.

$$\Delta T = \frac{T_{max_1} - T_{max_2}}{T_{max_2} - 135} \quad 40$$

Where, T_{max_1} is the maximum temperature of Si wafer for the given grid and T_{max_2} is the maximum temperature of the Si wafer from the baseline grid.

5.2 Direction of heat transfer:

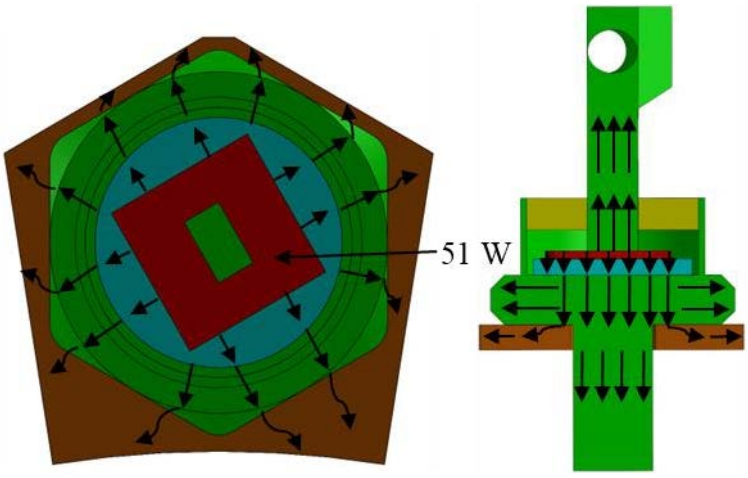

Figure 22: Direction of heat transfer from Si Wafer.

Based on the simulation results, it was observed that a significant portion of the heat generated was transferred to the diode casting and the copper bus bar. In the preliminary cases, approximately 70% of the thermal load was directed towards the diode casting, while 29% was absorbed by the bus bar. However, with the final design, these percentages shifted to 76% for the diode casting, 17% for the bus bar, and about 2% for the terminal lug. This change can be attributed to the reduction in size of the bus bar, resulting in a greater proportion of the thermal losses absorbed by the diode casting.

5.3 Preliminary geometry results

The 2 mm nozzles geometry and 0.5 mm nozzle geometry were run with four different configurations keeping the total flow rate constant. In first configuration all three nozzles were turned on. The second configuration used one of the two horizontally aimed nozzles. The third configuration used the angled nozzle, while the fourth configuration used the two horizontally aimed nozzles. The comparison was done based on the maximum temperature of the silicon wafer and pressure drop across the nozzle required for each configuration. The maximum temperatures from 2 mm and 0.5 mm nozzle with all four configurations are shown below.

5.3.1 Three nozzles

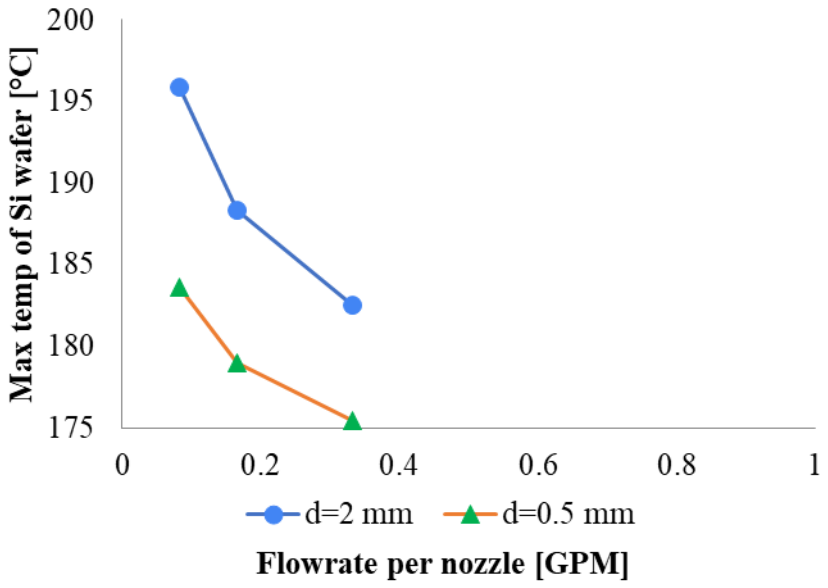

Figure 23: Maximum Temperatures with three nozzles.

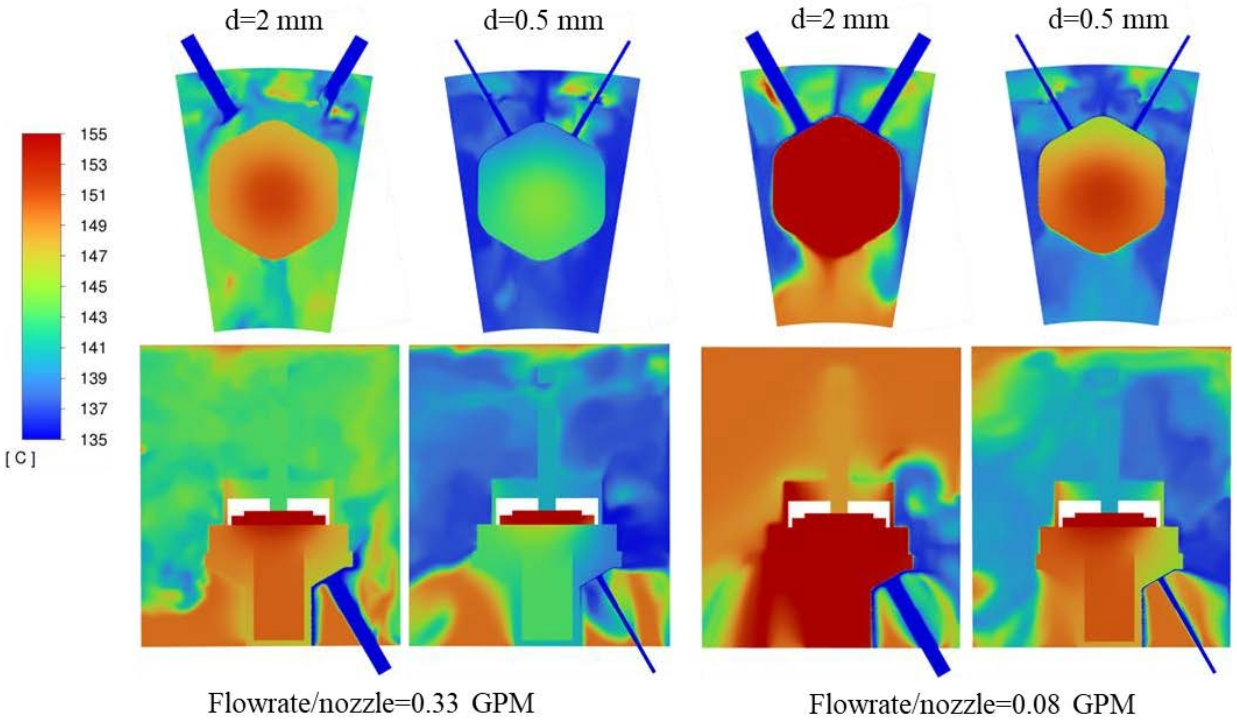

Figure 24: Temperature Contour with three nozzles for 2 mm and 0.5 mm nozzles.

5.3.2 One Straight Nozzle

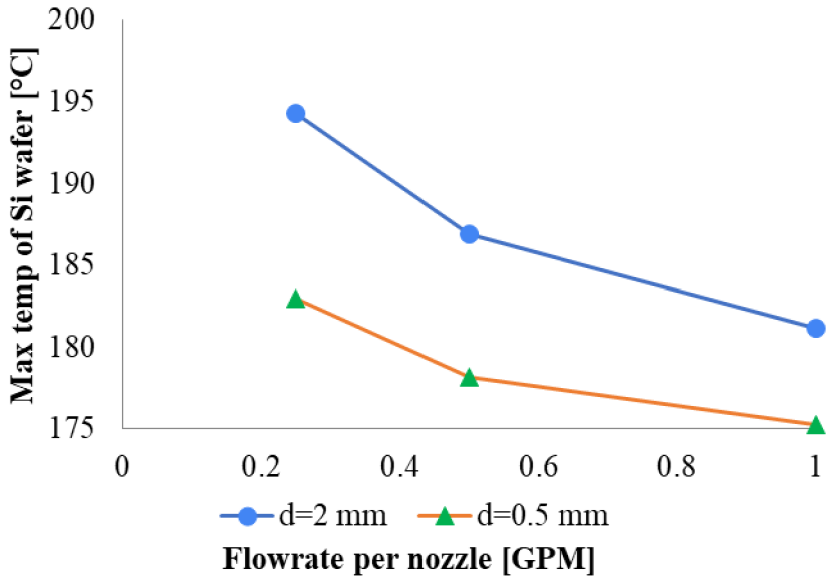

Figure 25: Maximum Temperatures with one straight nozzle.

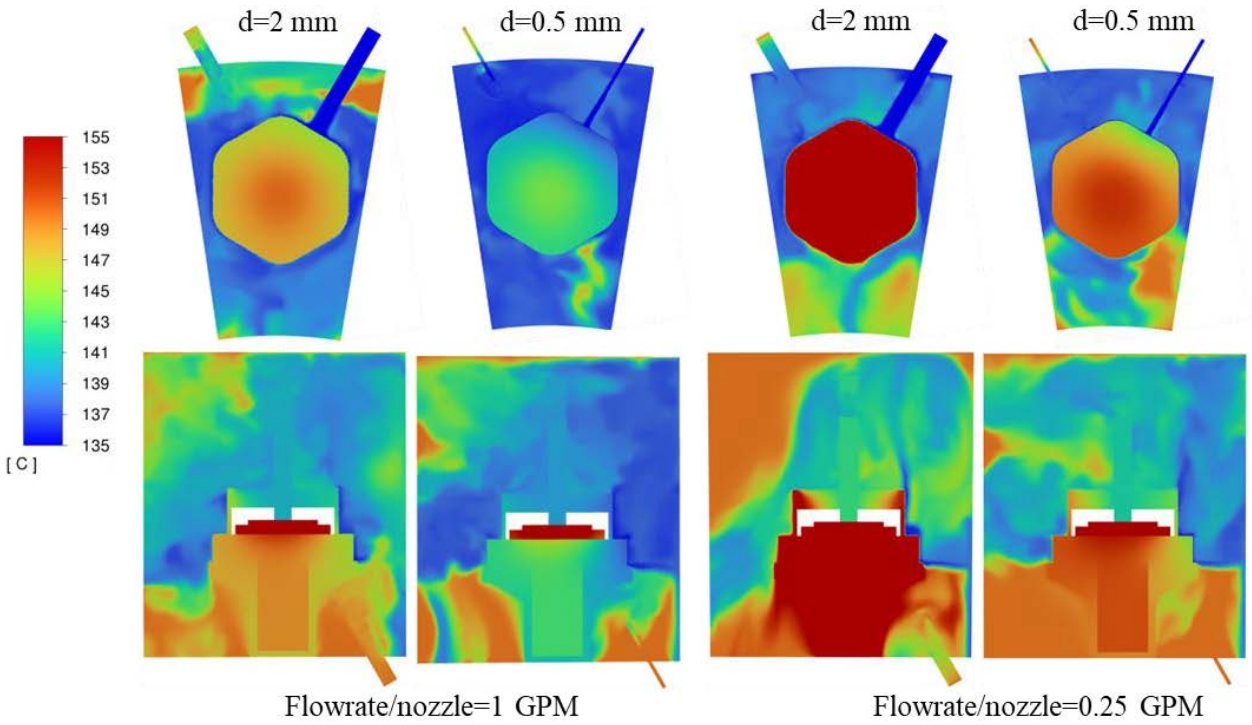

Figure 26:Temperature Contour with one straight nozzle for 2 mm and 0.5 mm nozzles.

5.3.3 Angled Nozzle

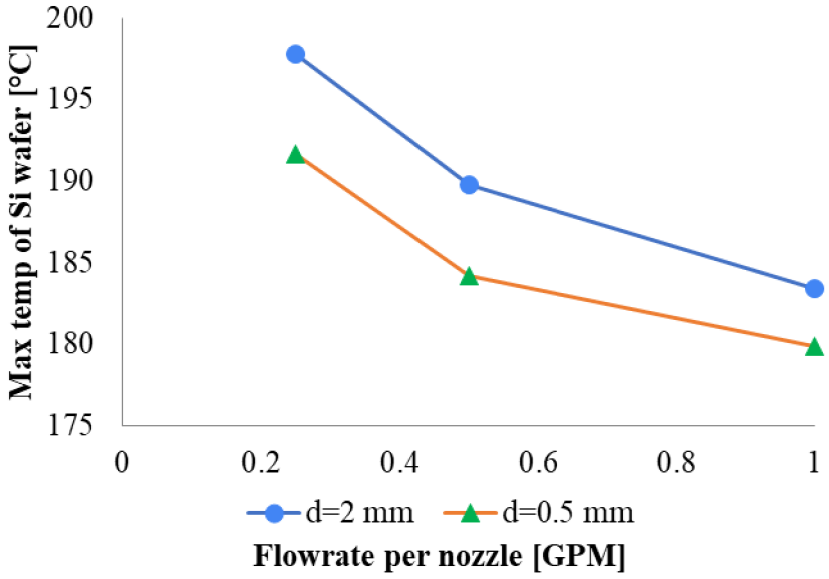

Figure 27: Maximum Temperatures with angled nozzle.

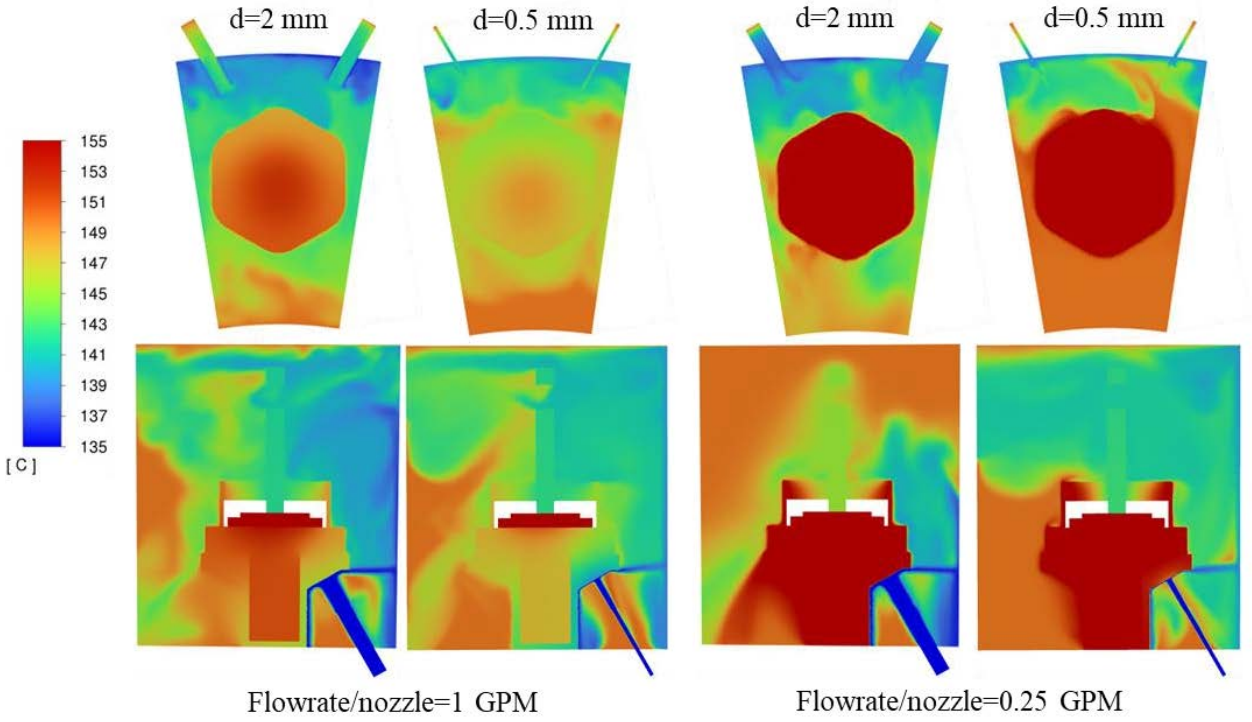

Figure 28:Temperature Contour with one straight nozzle at 1 GPM and 0.25 GPM.

5.3.4 Two Straight Nozzles

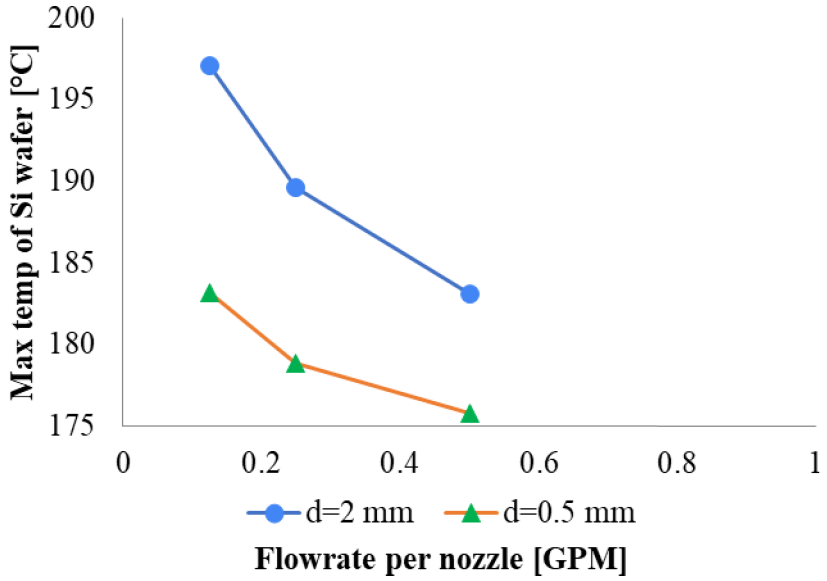

Figure 29: Maximum Temperature with two straight nozzle configurations

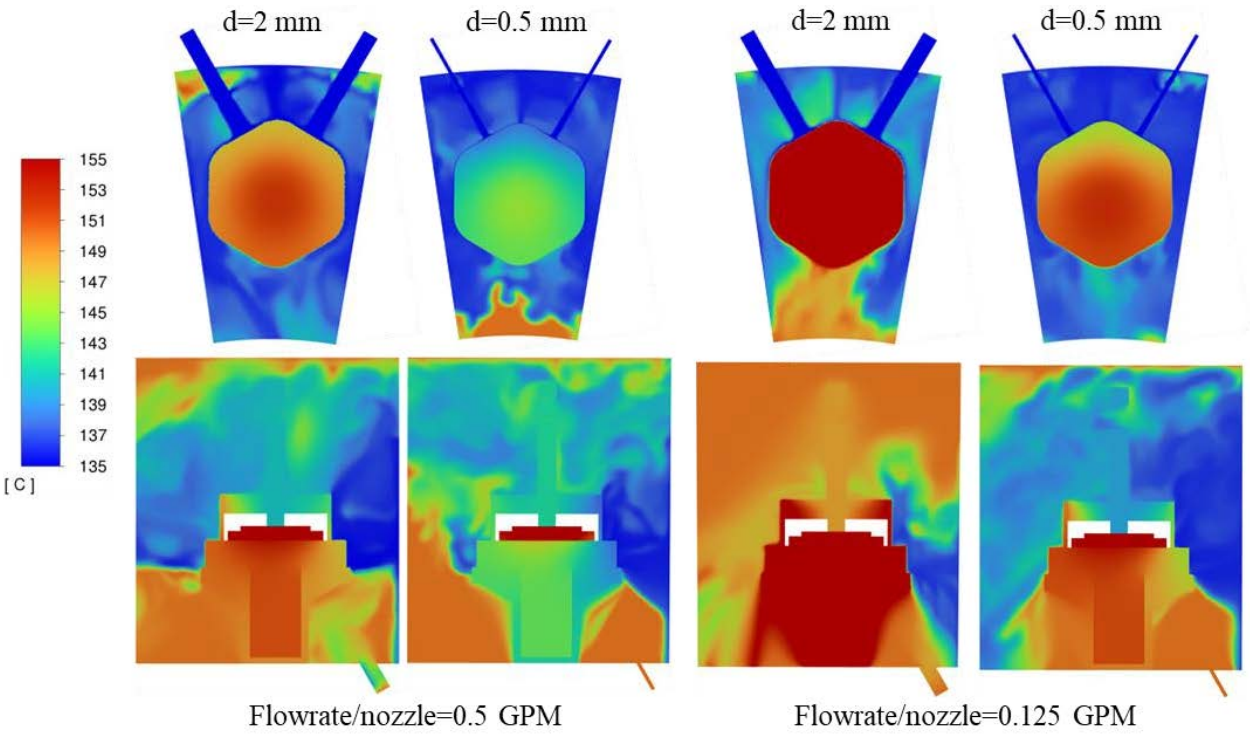

Figure 30:Temperature Contour with two straight nozzles at 1 GPM and 0.25 GPM.

5.3.5 Effects of nozzle configuration and number of nozzles

The results indicate that among the four configurations, the angled nozzle yielded the least favorable outcomes in terms of maximum temperature. On the other hand, one of the straight nozzles performed well and achieved the best cooling results. When comparing the results from various configurations of 2 mm and 0.5 mm nozzles on the same graph, a notable observation emerges: the angled nozzle for the 0.5 mm diameter shows a significantly higher temperature compared to the other configurations.

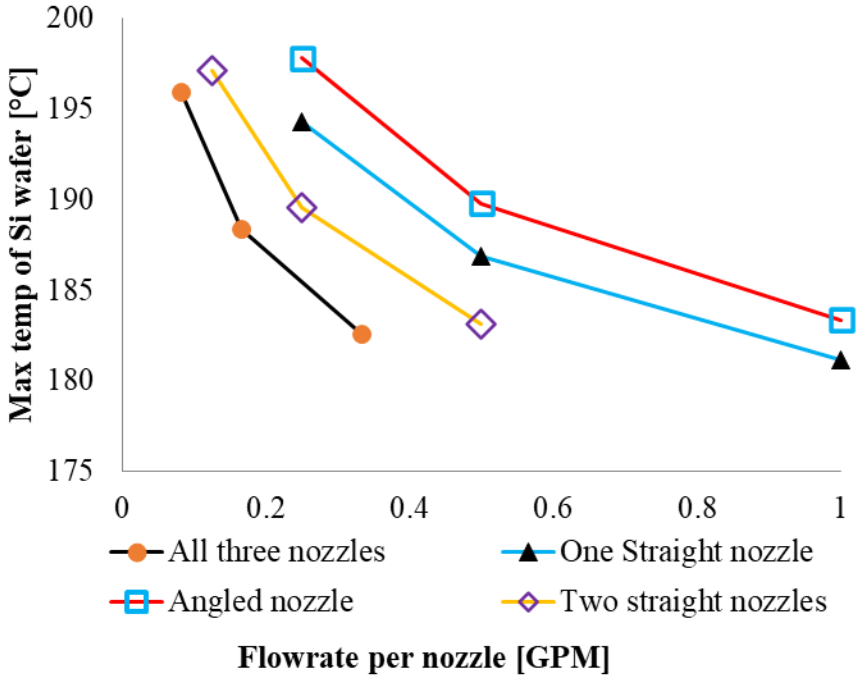

Figure 31: Maximum Temperature from all configurations for 2 mm nozzle at different flow rate.

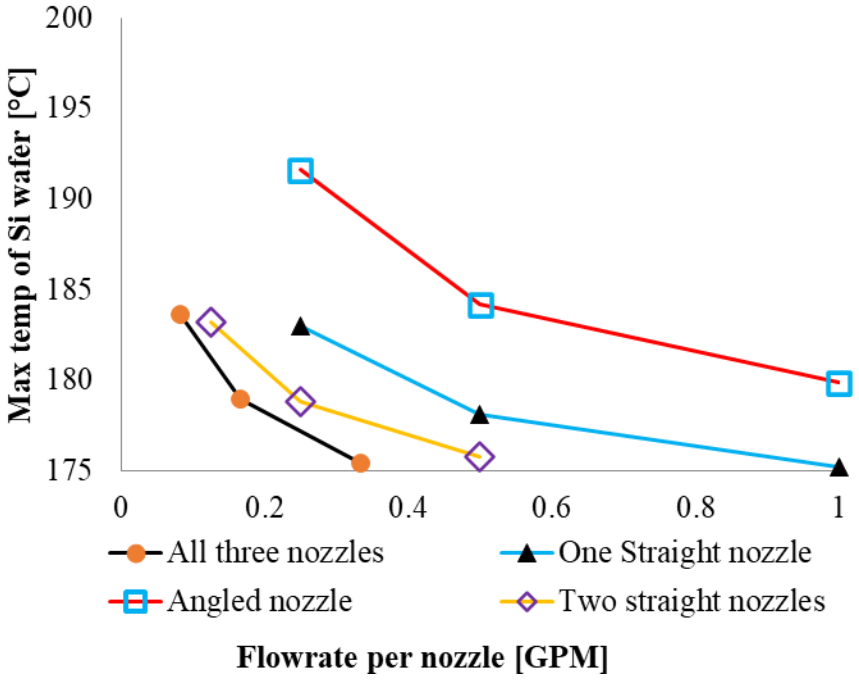

Figure 32: Maximum Temperature from all configurations for 0.5 mm nozzle at different flow rate.

The inferior thermal performance of the 0.5 mm angled nozzle can be attributed to the inadequate delivery of oil to the diode surface illustrated in Figure 33. This deficiency hampers the diodes' ability to effectively transfer heat to the incoming oil jet.

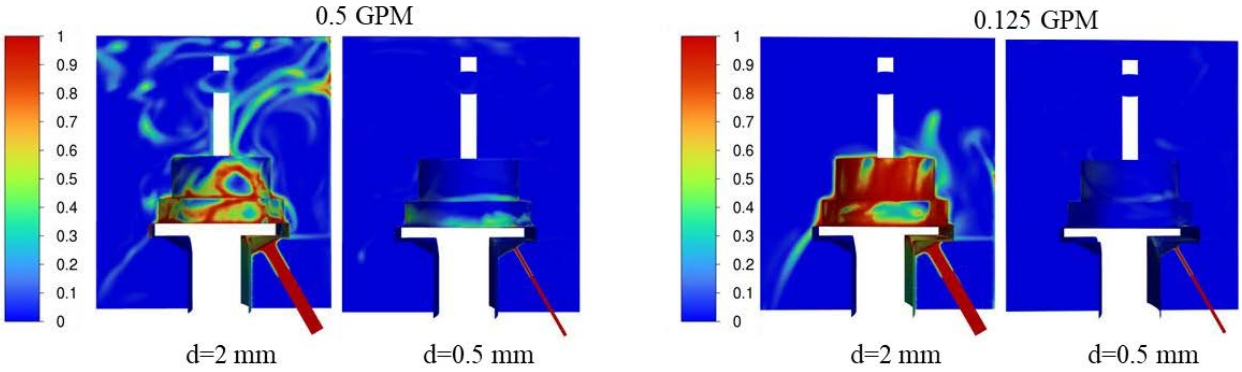

Figure 33: Volume fraction of oil with angled nozzle at 1 GPM flowrate.

However, it was also important to consider the pressure drop when selecting the optimal configuration. The pressure drop across the nozzles during the preliminary study is shown below:

Table 5-2: Maximum pressure drop through each case from preliminary study.

All three nozzles			One straight Nozzle			Angled nozzle			Two straight nozzles		
Flow rate per nozzle [GPM]	Max pressure drop [psi]		Flow rate per nozzle [GPM]	Max pressure drop [psi]		Flow rate per nozzle [GPM]	Max pressure drop [psi]		Flow rate per nozzle [GPM]	Max pressure drop [psi]	
	d=2 mm	d=0.5 mm		d=2 mm	d=0.5 mm		d=2 mm	d=0.5 mm		d=2 mm	d=0.5 mm
0.33	1.2	463.0	1	7.6	3443.7	1	7.7	3407.3	0.5	2.2	960.9
0.17	0.5	145.8	0.5	2.2	980.2	0.5	2.2	961.2	0.25	0.9	279.7
0.08	0.2	53.2	0.25	0.9	280.8	0.25	0.9	279.9	0.125	0.3	94.3

While pressure drop through the nozzle was not initially a constraint in the project, it would still be preferable to have a lower pressure drop. This is because in an aerospace generator,

it is anticipated that there are other components that use the same cooling oil and supplied pressure is limited. By minimizing the pressure drop across the nozzle, it ensures that a significant portion of the pressure is retained for efficient operation of the other components in the system. From Table 5-2, it is clear that one nozzle configuration produced the highest pressure drop which confirms that pumping power requirement will be higher. On the other hand, the three nozzles configuration produced decent results in terms of temperature, but having a nozzle coming at an angle will complicate the manufacturing process. Straight nozzles can be easily drilled or bored using standard drilling or milling process which are well-established and widely available. On the other hand, drilling angle holes raises issues like securing stock material in correct position, requirement of expensive tools, and inaccuracy might arise. Thus, to keep manufacturing as simple as possible and to reduce the pumping pressure the two straight nozzle configuration was chosen.

5.3.6 Effects of nozzle diameter

An additional observation that emerges distinctly from the results is that at a given flowrate, the cooling performance of the smaller nozzle (0.5 mm) was better than the bigger nozzle (2 mm). This can be credited to the higher impinging power that 0.5 mm diameter produces.

Table 5-3: Dimensionless Impingement power per nozzle for 2mm and 0.5 mm nozzles.

Flow rate per nozzle [GPM]	Dimensionless impinging power per nozzle	
	d=2 mm	d=0.5 mm
0.5	4.18E+09	1.07E+12
0.25	5.22E+08	1.34E+11
0.125	6.53E+07	1.67E+10

The dimensionless impingement power of the 0.5 mm nozzle was 256 times greater than that of 2 mm nozzle at a given flowrate. Higher impingement power results in efficient heat transfer improving the cooling performance, however it might not always be beneficial. Along with the risk of damaging the target surface (due to excessive stress), high impingement power comes with high energy consumption. This impacts the overall efficiency and operational cost of the system. So, while designing an impinging jet cooling system, it is necessary to lower the impinging power without compromising heat transfer performance to reduce the overall cost. Comparison of the two nozzle diameters in question at the same impinging power is shown in Figure 34. which clarifies the influence of impinging power.

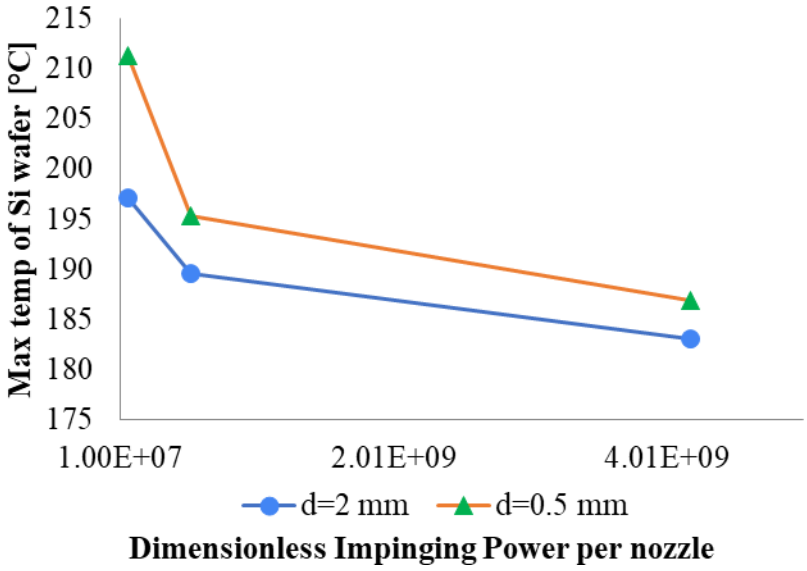

Figure 34: Comparison of max temperatures between 2 mm and 0.5 mm nozzle at the same impinging power.

The 2 mm nozzle outperforms the 0.5 mm nozzle even though the impinging power was the same. The better performance of 2 mm diode was because of the larger diameter being

able to cover more surface area of the diode as seen in Figure 35. This means that at the same flow rate condition, 0.5 mm nozzle will result in better cooling of the diode but higher impinging power, while at the same impinging power the 2 mm nozzle produces lower temperatures but at higher flow rates which requires larger pumping power. The table below shows the corresponding flowrate per nozzle at the given impinging power.

Table 5-4:Flow rate per nozzle for 2mm and 0.5 mm nozzles.

Dimensionless Impinging power per nozzle (IP*)	Flow rate per nozzle [GPM]	
	d=2 mm	d=0.5 mm
4.18E+09	0.5	0.08
5.22E+08	0.25	0.04
6.53E+07	0.125	0.02

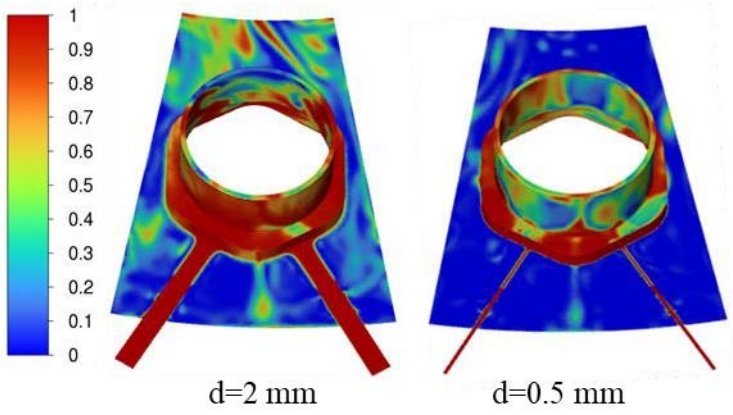

Figure 35: Volume fraction of oil at IP 4.18E+9.*

5.4 Final design results

From the learnings of preliminary research, a systematic pursuit of design refinements was done to achieve optimal performance, efficiency, and functionality, while meeting the

desired standards and constraints. The main geometric difference was the diameter of the nozzle which was changed to 0.762 mm. This was the minimum spacing required between the heat sink and the manifold. The surface of the bus bar facing the jets was carefully angled to match the inclination of the target surface.

Figure 36 showcases the results obtained for the 0.762 mm diameter nozzle at a specific nozzle-to-target spacing of 2 for flow through one nozzle and two nozzles.

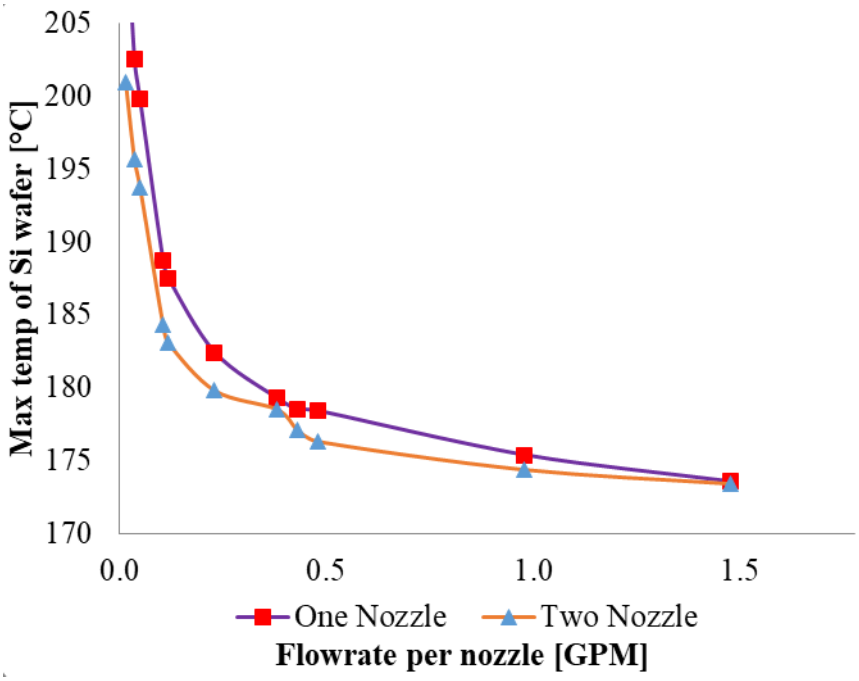

Figure 36: Maximum temperature of Si Wafer at various flow rates for 0.762 mm nozzle at h/d=2.

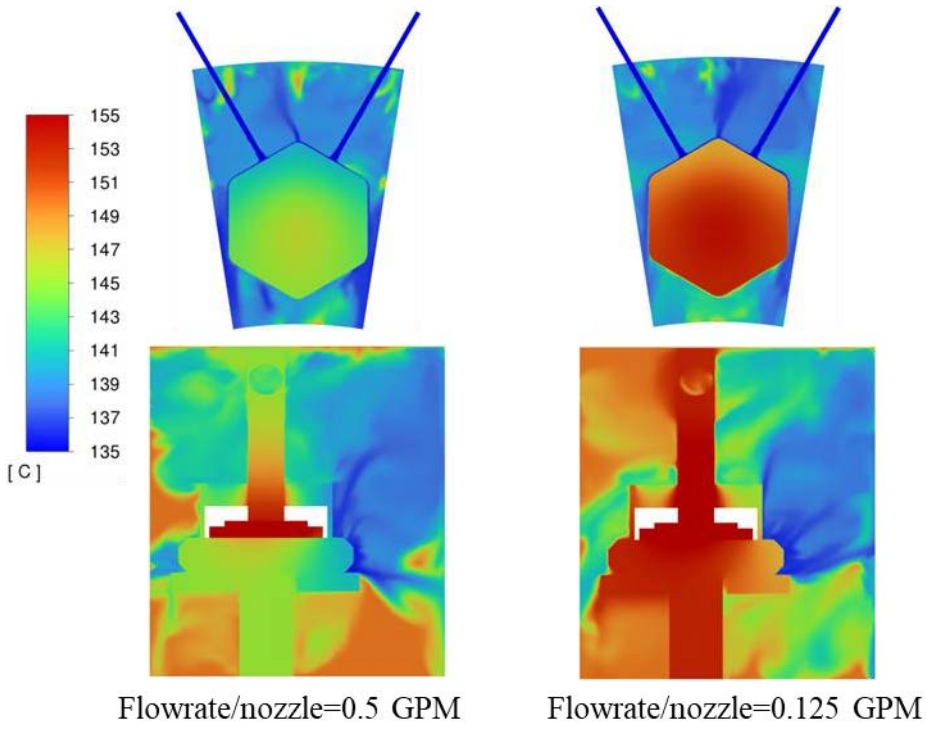

Figure 37: Temperature contour for 0.762 mm nozzle with flow through 2 nozzles.

The influence of two nozzles on the flow rate was found to be more significant as the flow rate decreased. For the highest flow rate tested (1.5 GPM per nozzle) the difference in temperature was 0.14°C while at the lowest flowrate (0.03 GPM per nozzle) the was 12.07°C. This finding suggests that the use of multiple nozzles can cool the diode more effectively.

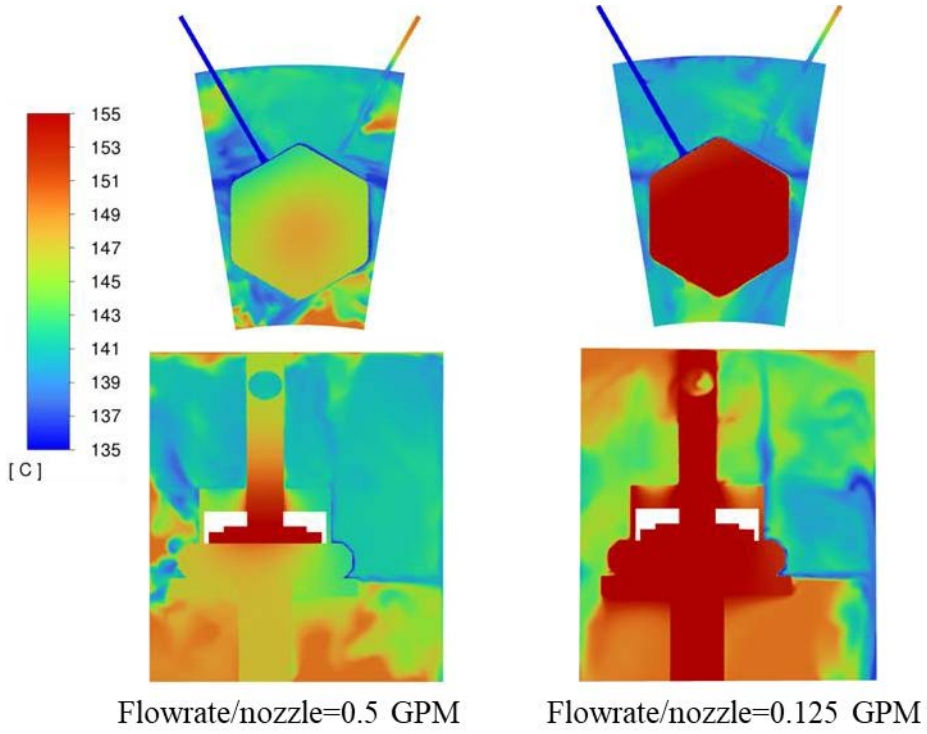

Figure 38:Temperature contour for 0.762 mm nozzle with flow through one nozzle.

5.4.1 Effects of nozzle to plate spacing

In the field of impinging jet applications, a comprehensive examination of the impact of nozzle-to-target spacing is of utmost importance. In the current study, negligible effects of nozzle-to-target spacing on the maximum temperature of the silicon wafer was observed. The change in maximum temperature was found to be minimal, indicating that this particular parameter has limited influence on the overall outcome. The comparisons were done at the same dimensionless impinging power that the preliminary models were compared at in section 5.3.6.

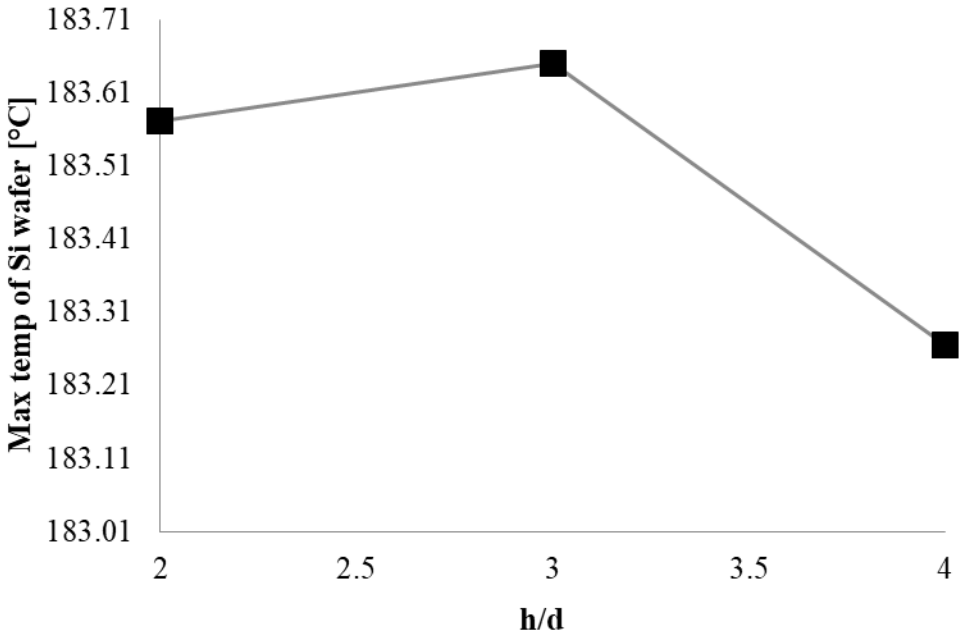

Figure 39: Maximum Temperature at IP=4E+10 and Flowrate=0.069 GPM per nozzle for three different spacing.*

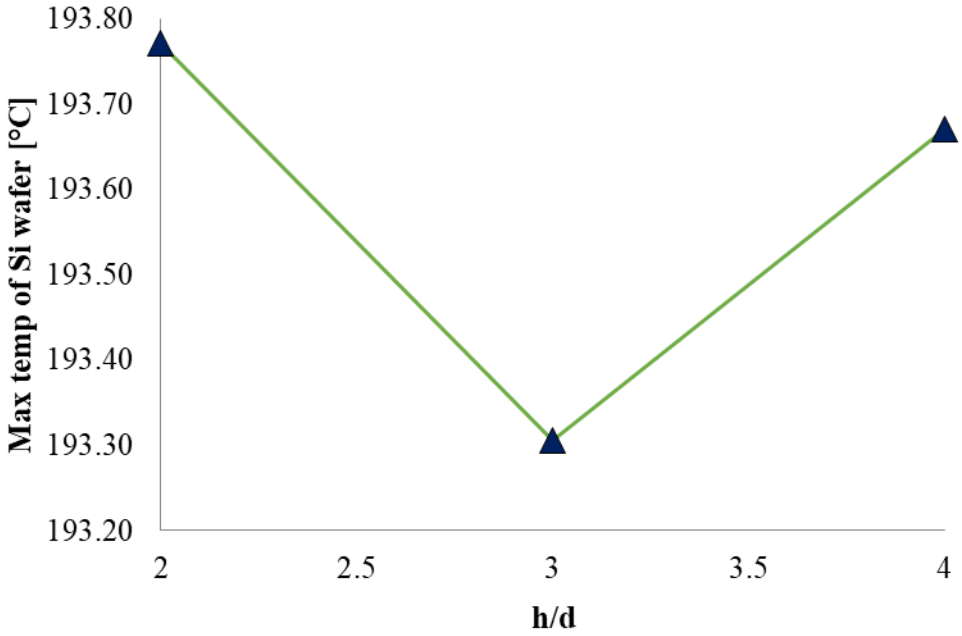

Figure 40:Maximum Temperature at IP=5E+8 and Flowrate=0.035 GPM per nozzle for three different spacing.*

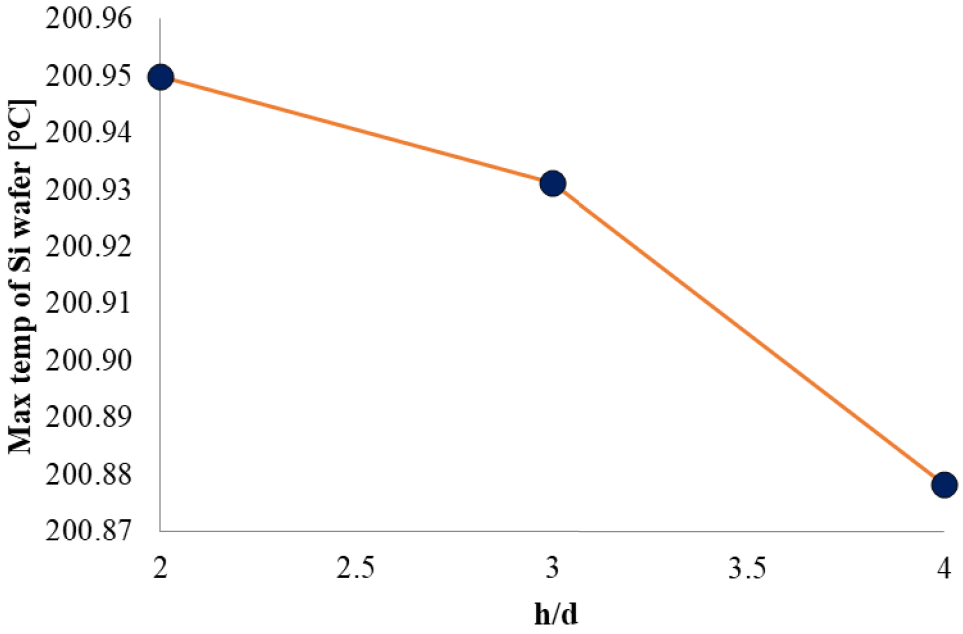

Figure 41:Maximum Temperature at IP=6E+6 and Flowrate=0.017 GPM per nozzle for three different spacing.*

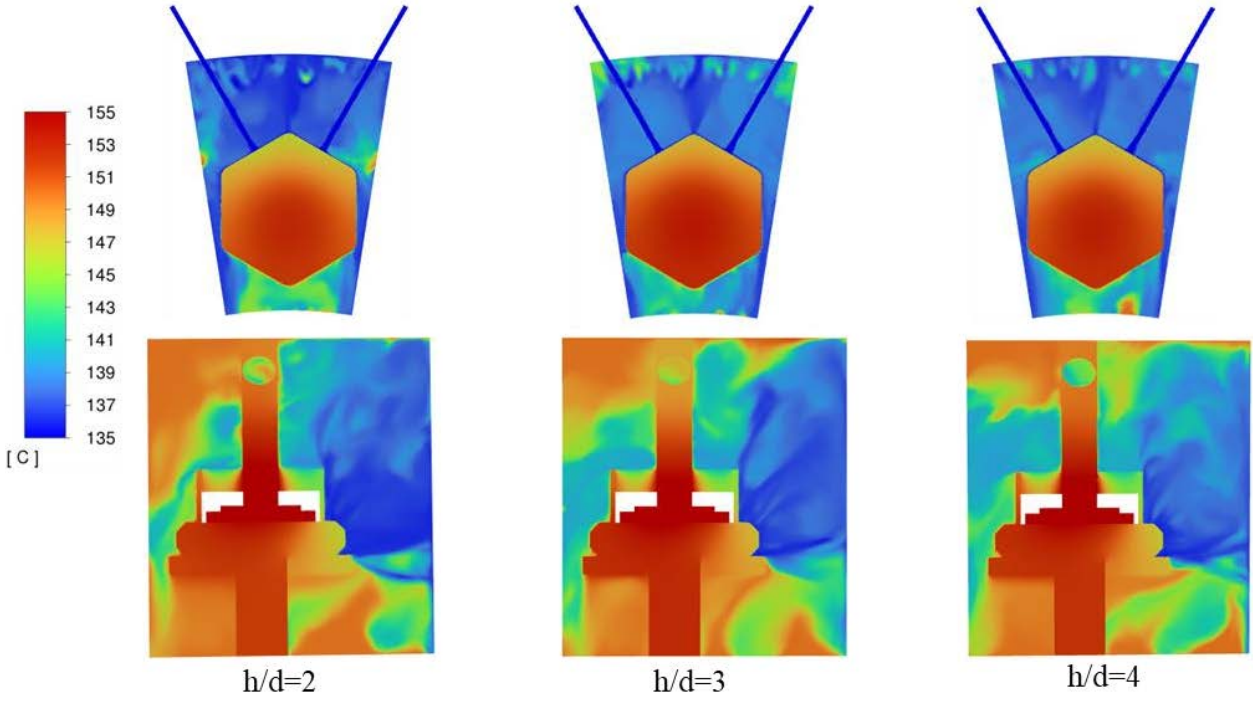

Figure 42:Temperature Contours for 0.762 mm nozzle at IP=4E+10 and flowrate=0.069 GPM per nozzle for three different spacing.*

5.4.2 Effects of manifold walls

To investigate the influence of manifold walls on the maximum temperature of the Si-wafer, the manifold walls shown in Figure 12 were incorporated as solid bodies in the simulation. Three different flow rates through two nozzles at h/d=2 were compared to the case where manifold were not present. The results are presented below.

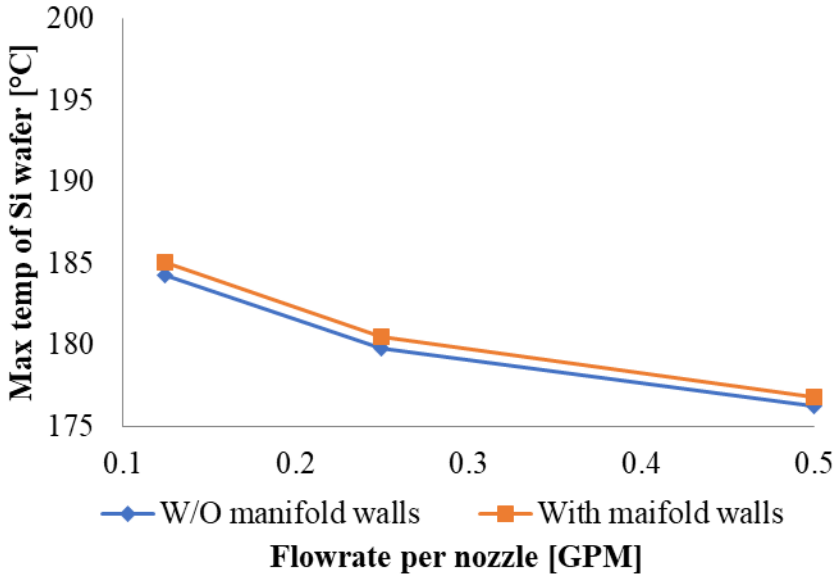

Figure 43: Comparison of maximum temperature of Si wafer w/o and with manifold walls.

The results suggest a slight increase in the maximum temperature of the Si-wafer temperature. However, it is important to note that the difference is less than 1°C.

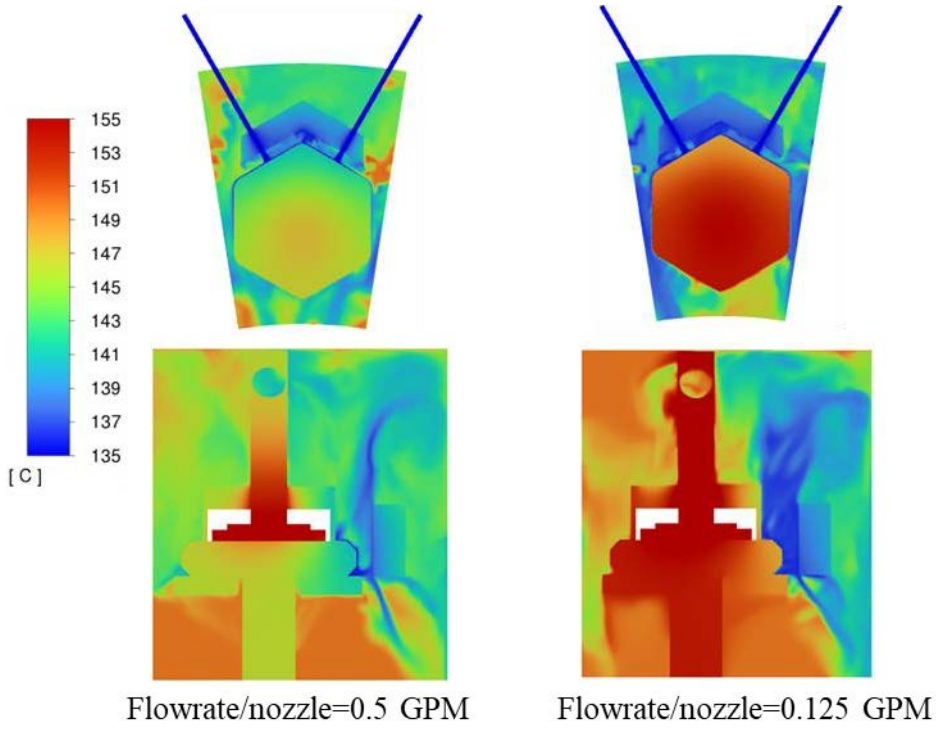

Figure 44: Temperature contours for 0.762 mm nozzle w/o and with manifold walls.

5.4.3 Stagnation Point Nusselt Number

The Nusselt number at the stagnation point for target 1 was also measured using equation (27). To do so, a point at the stagnation point was established in FLUENT and the maximum heat flux at that point was evaluated. Additionally, the maximum surface temperature at the stagnation point was also accessed and incorporated into equation (25). It is important to note that the reference temperature for all cases was the temperature of the oil at the inlet. The Nusselt number from the simulations were compared with the co-relation provided by [7] [25].

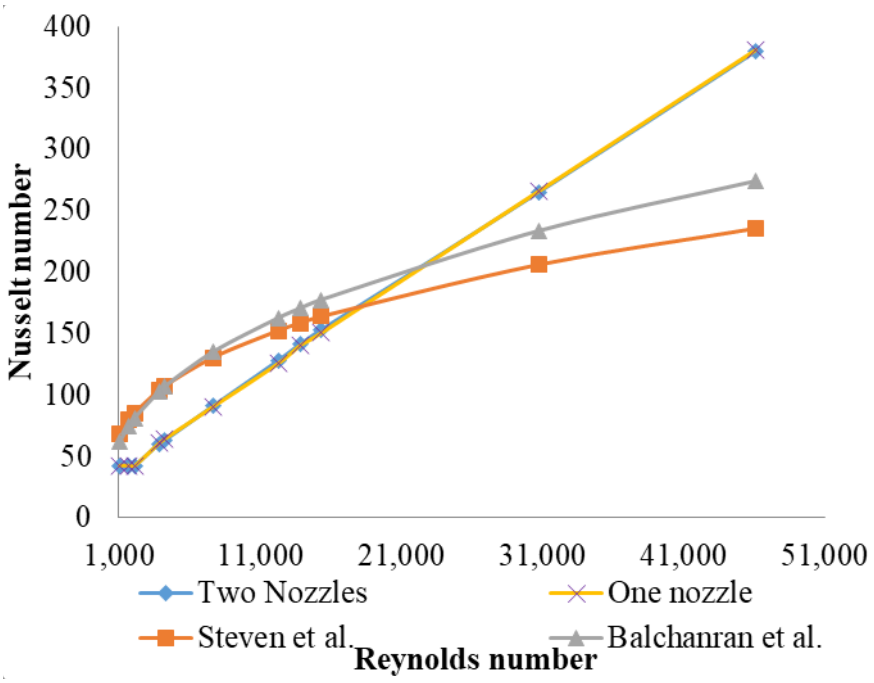

Figure 45: Nu number comparison with literature for 0.762 mm nozzle.

The experimental works of [7] and CFD analysis of [25] show power law relationship between the Reynolds number and Nusselt number however, from the current analysis the relationship is quadratic. This discrepancy can be attributed to the differences in geometry. While the literature focused on a jet impingement on a flat plate. Although the targets were flat the current study considers a more complex diode geometry. Furthermore, the gravity in the current analysis does not align with the direction of jet.

Oil was flowed through only one nozzle as one could say that the interference between the two jets might introduce variation in the Nusselt number. This interference was eliminated, and Nu numbers were calculated at the same location. As the figure above suggests the interference between the jets had minimal impact on the stagnation point Nu number. This finding is noteworthy as it implies that two jets impinging on two different target surfaces in close proximity does not affect the heat transfer rate at the stagnation point.

In the previous studies [7] and [25], the flats plates were maintained at constant heat condition. However, in the current simulation incorporating the diode, we deviated from the approach of employing constant heat flux or constant temperature boundary conditions at the targets. Instead, a remote heat source in the form of a Si wafer was introduced. Thus, conduction takes place within the diode component, while convection occurs at the target due to the presence of jets. This avoids diode form getting cooled uniformly as evident in the following figure.

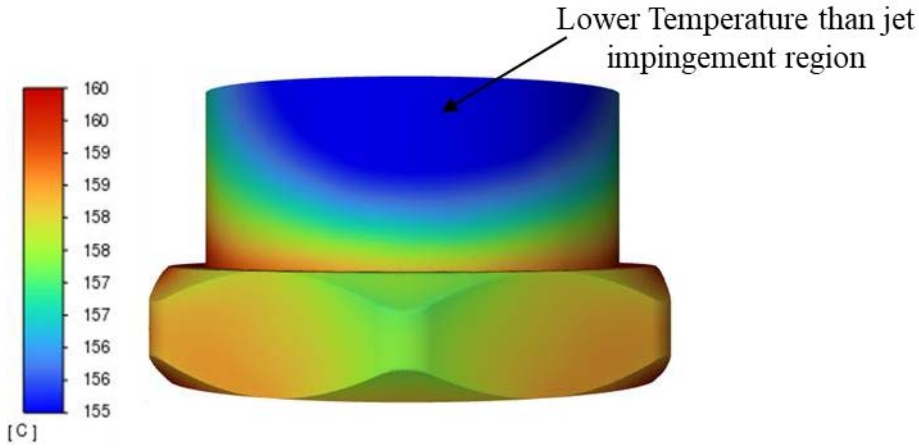

Figure 46: Temperature distribution on the diode casting.

It was also seen that the location where two jets interacted in the case of flow through two nozzle exhibited lower temperature. Another reason why this location is colder was because it was farther from the Si wafer compared to the target surfaces.

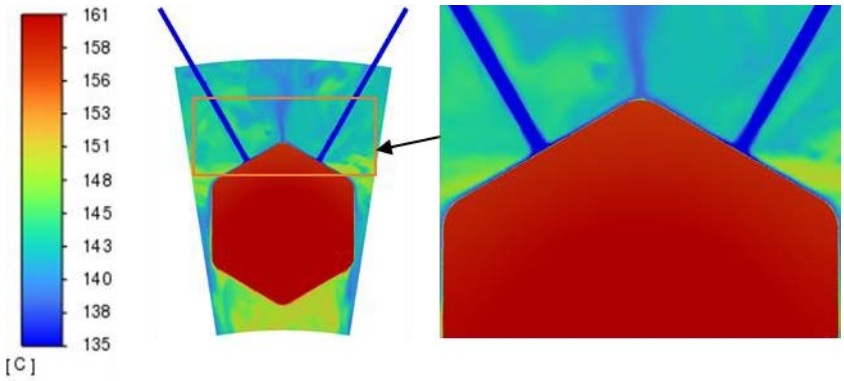

Figure 47: Temperature contour for 0.762 mm at IP and 0.07 GPM.*

Extensive exploration of the available literature reveals h/d exerts a minimal influence on the stagnation point Nusselt number at constant Reynolds number [20] [21] [25]. This finding is further confirmed by the outcomes derived from our current analysis as shown in figure.

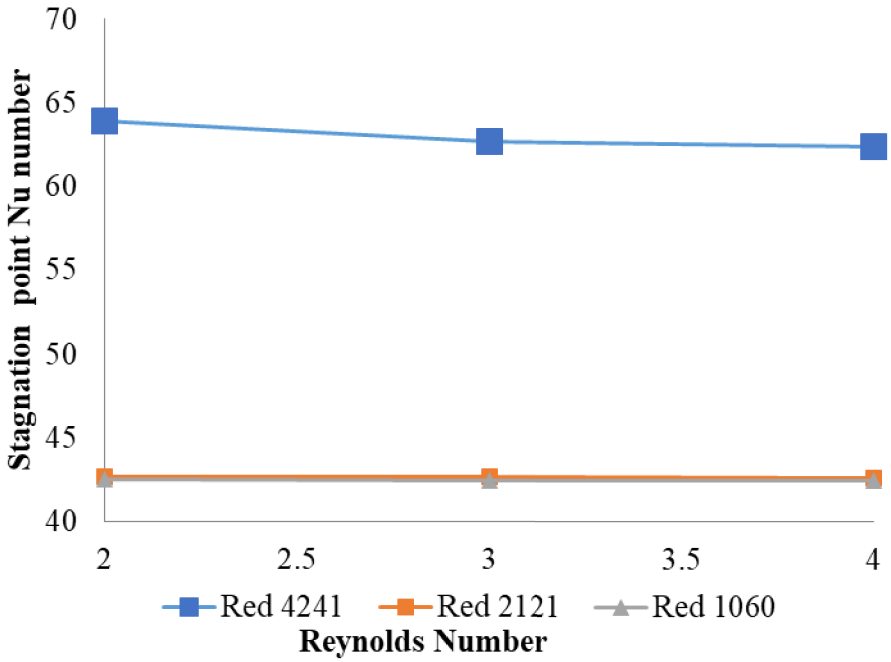

Figure 48:Stagnation point Nu number at three different spacing with two active nozzles

6 Manufacturable Model

A manufacturable model was proposed based on the finding of the simulation. The nozzle to target spacing was maintained at 2 as no significant changes in the maximum temperature of the Si wafer was seen at h/d of 3 and 4.

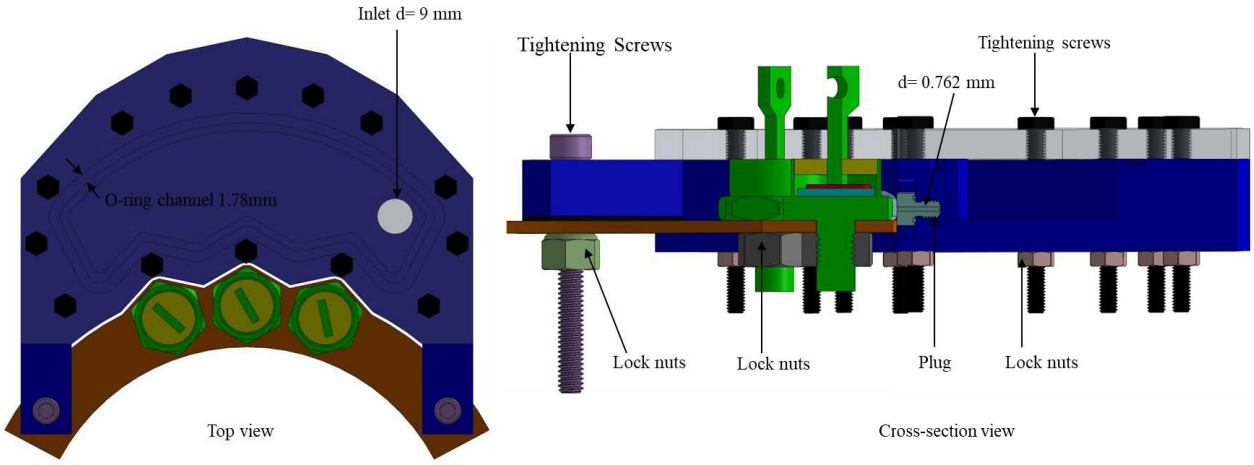

Figure 49: Final Manufacturable Model.

The model consisted of a manifold with an inlet, O-ring channel, and plugs for the oil to impinge on the diode target surfaces. Additionally, a manifold cover was also built, and all the components were secured using tightening screws and luck nuts of various sizes.

The pictures of the components that were machined are included in the Appendix along with their drawing.

7 Conclusion

1. Findings suggest that the choice of nozzle diameter can significantly impact the cooling efficiency of the jet. A larger nozzle diameter was found to have noticeable effects, as it effectively covers a greater surface area of the diode, resulting in a higher heat transfer rate.
2. At identical flowrate conditions, the impinging power is of greater significance as the smaller diameter nozzle generates higher impinging power compared to the larger diameter nozzle thus produce better cooling efficiency.
3. A compromise between cooling capacity and pumping power is needed which will impact the nozzle size and required flowrate.
4. At lower flowrate multiple nozzles have been found to significantly enhance the cooling capacity of the system by distributing the oil more efficiently.
5. Diode is not cooled uniformly due to conduction within the diode and convection due to the jets, also heat distribution within the system was not uniform.
6. The interference between the jet do not impact the heat transfer coefficient or the Nu number at the stagnation point of the target.
7. Upon investigating the rage of h/d (2 to 4), no significant impact on the maximum temperature of Si wafer was found.

8 Future Work

1. In order to ensure the accuracy of the simulation results, it is important that they are validated through a scientific experiment.
2. Through rigorous experimentation, a co-relation needs to develop that quantifies the heat transfer coefficient at the target surface which will act as base for the future works involving impinging jets on non-uniform heat flux or temperature surfaces.
3. A wider range of h/d needs to be studied to be studied to understand the significance of nozzle-to-target spacing on the maximum temperature of Si wafer.

9 Bibliography

[1] N. Zuckerman and N. Lior, "Jet Impingment Heat transfer: Physics, Correlation, and Numerical Modeling," *Advances in Heat Transfer,* vol. 39, pp. 565-631, 2006.

[2] V. Madonna, P. Giangrande and M. Galea, "Electrical Power Generation in Aircraft: review, challenges and opportunities," *IEEE Transactions on Transportation Electrification,* vol. 4, no. 3, pp. 646-659, May 2018.

[3] K. Choo, B. K. Friedrich, T. D. Ford and A. Glaspell, "Experimental study of the hydrodynamics and heat transfer of air-assited circular water jet impinging a flat circular disk," *International Journal of Heat and Mass Transfer,* vol. 106, pp. 804-809, 2017.

[4] E. J. Watson, "The radial spread of liquid over a horizontal plate," *Journal of Fluid Mechanics,* vol. 20, pp. 481-499, 1964.

[5] X. Liu and J. Liengard, "Liquid jet impingingment heat transfer on a uniform flux surface," *The American Socienty of Mechanical Engineers,* vol. 106, pp. 523-530, 1989.

[6] J. Baonga, H. Louahlia-Gualous and I. M, "Experimental study of the hydrodynamics and heat transfer of free liquid jet impinging a flat circular heated disk," *Applied Thermal Engineering,* vol. 26, pp. 1125-1138, 2006.

[7] J. Steven and B. W. Webbs, "Local Heat Transfer Coefficients Under an Axisymmetric, Single-Phase Liquid Jet," *ASME J. Heat Transfer,* vol. 133, pp. 71-78, 1991.

[8] Y. Brechet and Z. Neda, "On the circular hydraulic jump," *American Journal of Physics,* vol. 67, no. 8, pp. 723-731, 1999.

[9] K. Choo and S. Kim, "The influence of nozzle diameter on the circular hydraulic jump of liquid jet impingment," *Experimental Thermal and Fluid Science,* vol. 72, pp. 12-17, 2016.

[10] I. Tani and Y. Kamatsu, "Impingement of a round jet on a flat surface," *Applied Mechanics,* pp. 672-676, 1966.

[11] F. Giralt and C. T. O. Chia, "Characterization of the impingment region in an axisymmetric turbulent jet," *Industrial and Engineering Chemistry Fundamentals,* vol. 16, pp. 21-28, 1977.

[12] Y. Wang and R. E. Khayat, "The effects of gravity and surface tension on the circular hydrulic jump for low-and high viscosity liquids: A numerical Investigation," *Physics of Fluids,* vol. 33, pp. 012105-1-7, 2021.

[13] G. H. Raghav, "Numerical analysis of hydrulic jump by an impinging jet," 2014.

[14] L. Hosain, "CFD Simulation of Jet Cooling and Implementation of Flow Solvers in GPU," 2013.

[15] R. Balachandar, R. M. Barron and M. Shademan, "CFD analysis of the effect of nozzle stand-off distance on turbulent impinging," *Candaian Journel of Civil Engineering,* vol. 40, pp. 603-612, 2013.

[16] F. Giralt, C.-J. Chia and O. Trass, "Characterization of the Impingement Region in an Axisymmetric Turbulent Jet," *Industrial and Engineering Chemistry Fundamentals,* vol. 16, pp. 21-28, 1977.

[17] P. M. Brdlik and V. K. Savin, "Heat Transfer between an axisymmetric jet and a plate normal to the flow," *Journal of Engineering Phsyics,* vol. 8, pp. 91-98, 1965.

[18] H. Martin, "Heat and Mass Transfer between Impinging Gas Jets and Solid Surfaces," *Advances in Heat Transfer,* vol. 13, pp. 1-60, 1977.

[19] Z. H. Chaudhury, "Heat Transfer in radial liquid jet," *Jounal of Fluid Mechanics,* vol. 20, pp. 501-511, 1964.

[20] P. Y, S. J and W. B, "Effects of Nozzle Configuration on Transport in the Stagnation Zone of Axisymmetric, Impinging Free Surface Liquid Jets: Part 2-Local Heat Transfer," *Journal of Heat Transfer,* vol. 114, pp. 880-886, 1992.

[21] K. Choo, B. K. Friedrich, A. W. Glaspell and K. A. Schilling, "The influence of nozzle-plate-spacing on heat transfer and fluid flow of submerged jet impingement," *Experimental Thermal and Fluid Science,* vol. 97, pp. 66-69, 2016.

[22] J. W. Baughn and S. Shimizu, "Heat Transfer Measurements From a Surface With Uniform Heat Flux and an Impinging Jet," *Journal of Heat Transfer,* vol. 111, pp. 1096-1098, 1989.

[23] M. Behnia, P. A. Durbin and S. Parneix, "Prediction of heat transfer in an axisymmetric turbulent jet impinging on a flat plate," *Internal Journal of Heat and Mass Transfer,* vol. 41, pp. 1845-1855, 1998.

[24] M. Behnia, P. A. Durbin, S. Parneix and Y. Shabany, "Numerical study of turbulent heat transfer in con®ned and," *International Journal of Heat and Fluid Flow,* pp. 1-9, 1999.

[25] R. Balchandar, R. Barron, O. Iqbal and G. Nasif, "Simulation of Jet Impingment Heat Transfer," *ICEF 2013,* 2013.

[26] L. J. H, "Heat Transfer by Impingment of Circular Freee-Surface Liquid Jets," in *18th National & 7th ISHMT-ASME Heat and Mass Transfer Conference*, Guwahati, India, 2006.

[27] M. Behnia, S. Parneix and P. Durbin, "Accurate Modeling of impinging jet heat transfer," in *Center for Turbulence Research Annual Research Briefs 1997*, 1997.

[28] W. El-Maghlany, M. Sorour, A. Abbass and M. Alnakeeb, "Numerical Study of free surface axisymmetric jet impingment pn a heated flat surface utilizing high concentration SiO2 nanofluid," *Journal of the Taiwan Institute of Chemical Engineers,* vol. 135, no. 104401, 2022.

[29] ANSYS, "ANSYS Fluent User's Guide," 2013. [Online].

[30] K. Choo and S. J. Kim, "Heat Transfer and fluid fluid flow characteristics of two-phase impinging jets," *International Journal Heat and Mass Transfer,* vol. 53, pp. 5692-5699, 2010.

[31] L. S-bond Technology, "S-bond," 8 September 2002. [Online]. Available: https://www.s-bond.com/wp-content/uploads/assets/Documents/ProductBulletinSB220M.pdf. [Accessed 2023].

[32] Sobolewski M and Dziurdzia B, "Experimental approach to thermal conductivity of macro solder joints with voids," *Soldering & Surface Mount Technology,* vol. 31, pp. 181-191, 2019.

[33] K. Choo, S. I. Moldovan and K. A. M, "Heat Transfer and hydrodynamics of free water jet impingement at low nozzle-to-plate spacing," *International Journal of Heat and Mass Transfer,* vol. 108, pp. 2211-2216, 2017.

[34] M. Behnia, S. Parneix, Y. Shabany and P. A. Durbin, "Numerical study of turbulent heat transfer in confined and unconfined impinging jets," *International Journal of Heat and Fluid Flow,* pp. 1-9, 1999.

Appendix

Figure A1: Copper bus bar.

Figure A2: Manifold top view (left) and front view (right).

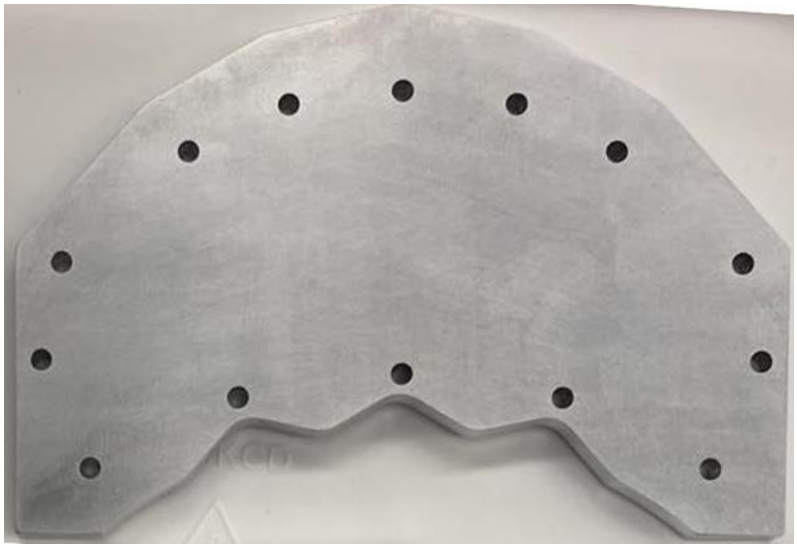

Figure A3: Manifold cover.

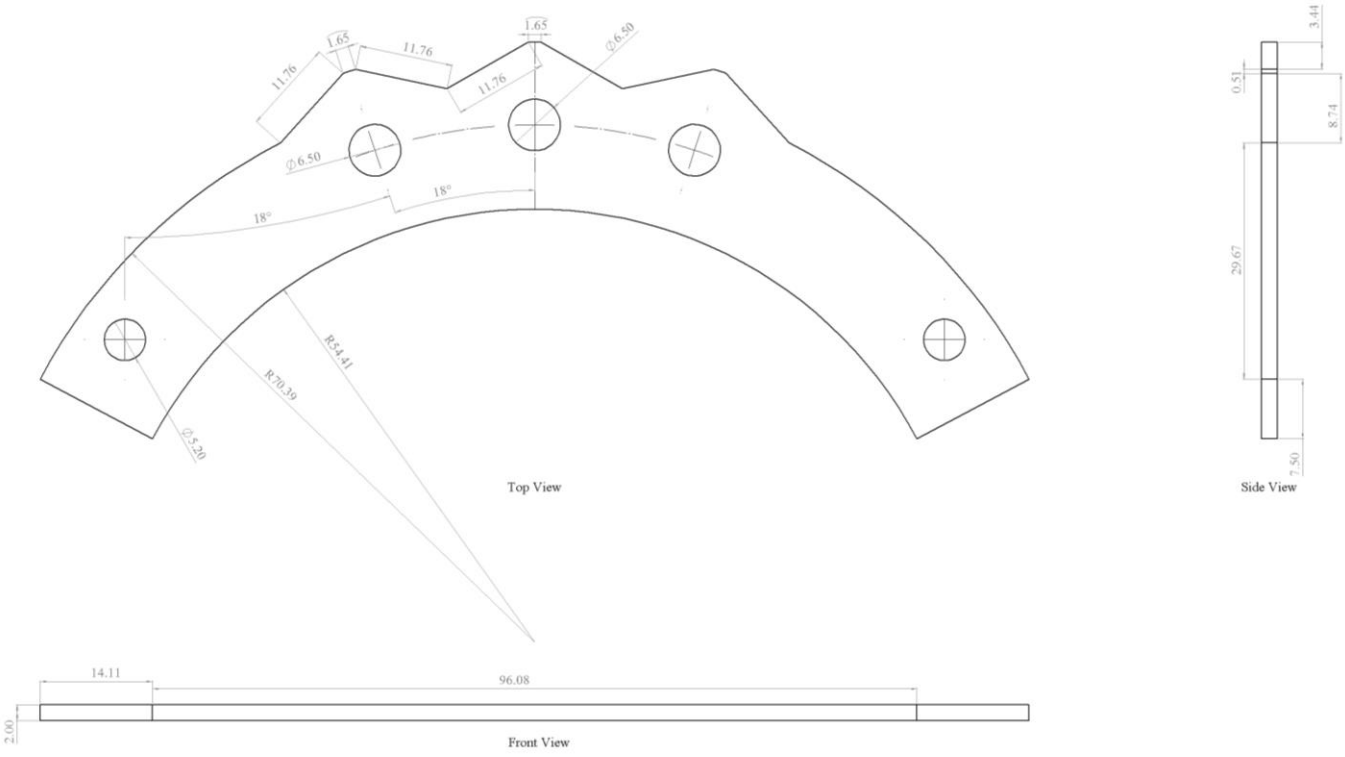

Figure A4: Copper bus bar drawing

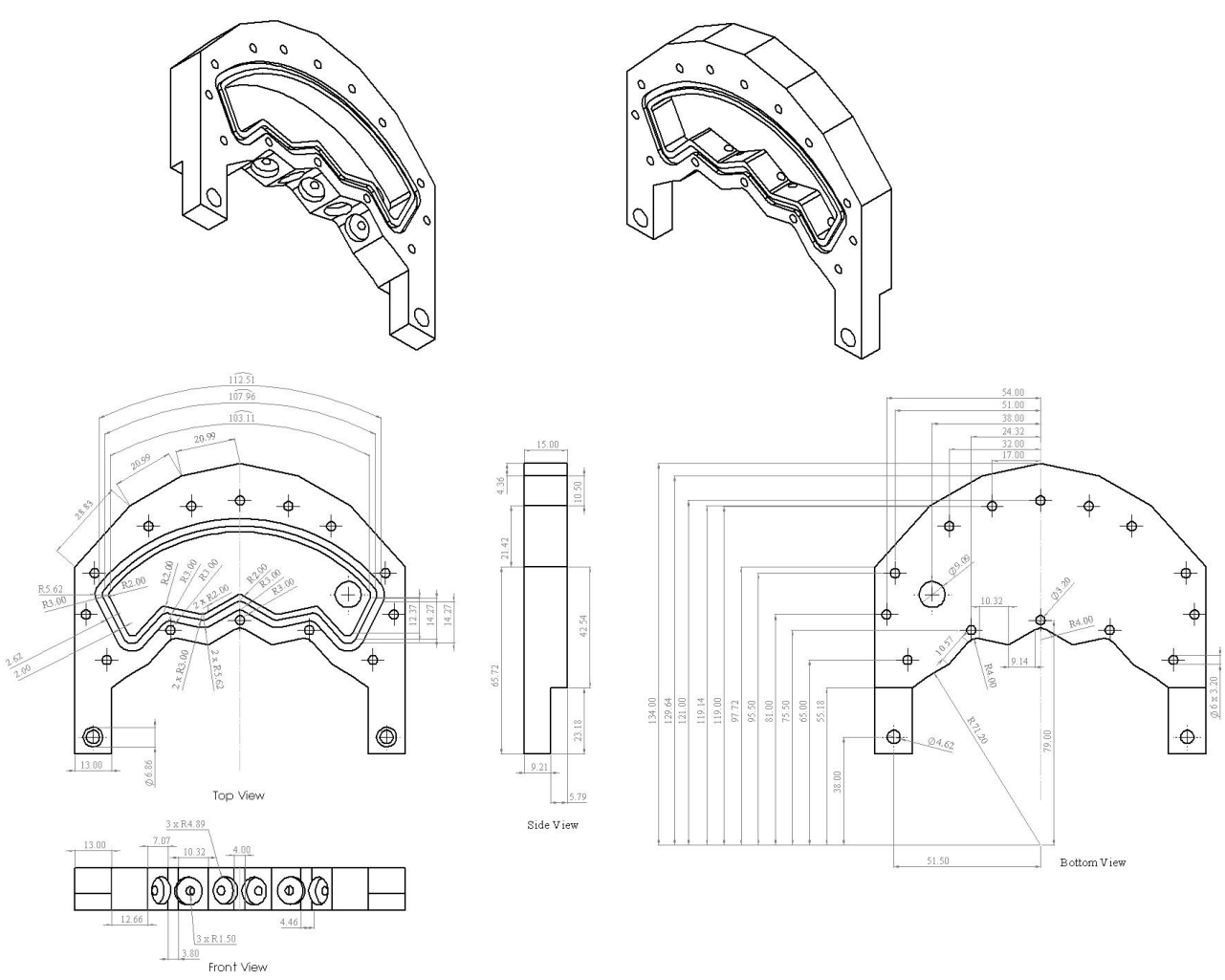

Figure A5: Manifold drawing

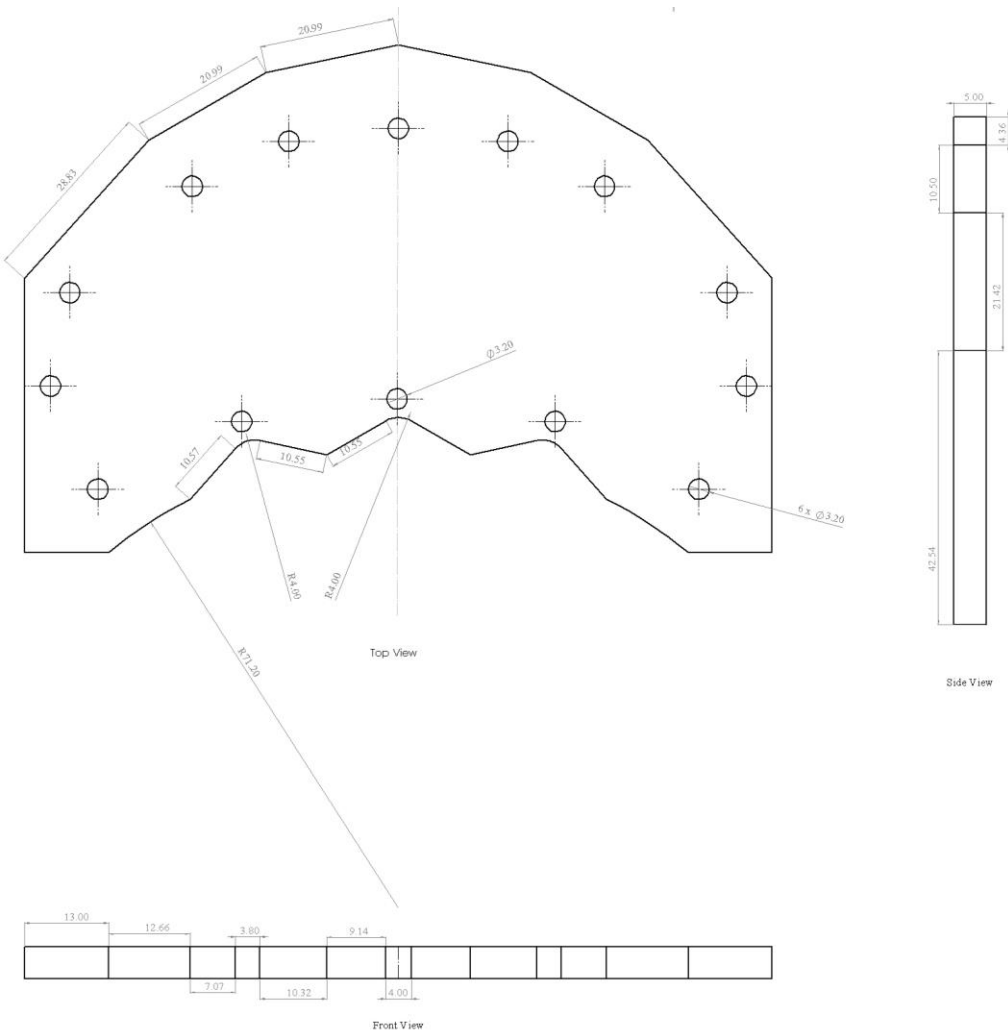

Figure A6: Manifold cover drawing